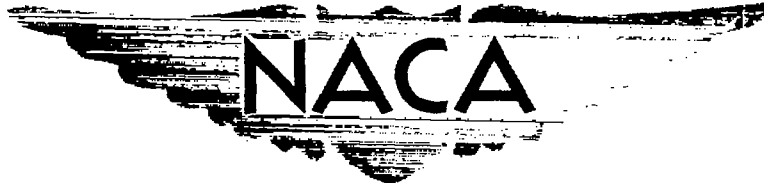


4204

Copy 226
RM L57J10

NACA RM L57J10

7808



JAN 29 1958

17448
17595

0144742



RESEARCH MEMORANDUM

MEASUREMENTS OF AERODYNAMIC HEAT TRANSFER ON A
15° CONE-CYLINDER-FLARE CONFIGURATION IN
FREE FLIGHT AT MACH NUMBERS UP TO 4.7

By Charles B. Rumsey and Dorothy B. Lee

Langley Aeronautical Laboratory
Langley Field, Va.

CLASSIFIED DOCUMENT

This material contains information affecting the National Defense of the United States within the meaning of the espionage laws, Title 18, U.S.C., Secs. 793 and 794, the transmission or revelation of which in any manner to an unauthorized person is prohibited by law.

NATIONAL ADVISORY COMMITTEE FOR AERONAUTICS

WASHINGTON

January 22, 1958

~~CONFIDENTIAL~~



NATIONAL ADVISORY COMMITTEE FOR AERONAUTICS

RESEARCH MEMORANDUM

MEASUREMENTS OF AERODYNAMIC HEAT TRANSFER ON A
15° CONE-CYLINDER-FLARE CONFIGURATION IN
FREE FLIGHT AT MACH NUMBERS UP TO 4.7

By Charles B. Rumsey and Dorothy B. Lee

SUMMARY

Measurements of aerodynamic heat transfer have been made at a number of stations along a cone-cylinder-flare model having a 15° total-angle conical nose and a 10° half-angle flare skirt. The maximum Mach number was 4.7, and local Reynolds numbers based on body length to a measurement station varied from 2×10^6 to 138×10^6 .

Local Stanton numbers measured on the nose cone and flare showed fair agreement with laminar and turbulent theories, while the measurements on the cylinder were generally somewhat lower than theory.

Experimental recovery factors, determined twice during the test, were unaccountably lower than theoretical values.

Local transition Reynolds numbers, based on length from the nose tip, varied from 3×10^6 to 18×10^6 and were much lower than values previously obtained on the smoother nose of a similar model.

At an angle of attack of about 9°, the heat transfer on the flare increased to more than twice the theoretical turbulent value for zero angle of attack.

INTRODUCTION

In the course of a program to investigate high-speed aerodynamic heat transfer, the National Advisory Committee for Aeronautics has flown several rocket-propelled research models designed to measure rates of skin heating at hypersonic speeds. Reference 1 reports such measurements on a 15° total-angle conical nose at Mach numbers up to 5.2. For

~~CONFIDENTIAL~~

the present test, a model of the same cone-cylinder-flare configuration was instrumented to obtain data along the cylindrical body and flare skirt as well as along the conical nose. In order to obtain data at Mach numbers up to 9 in this test, an additional booster stage was used with the three-stage propulsion system of the previous model, which reached a Mach number of 7. However, the motor of the last stage failed to ignite and the maximum Mach number of the test was 4.7. Free-stream Reynolds numbers per foot ranged from 3×10^6 to 16.5×10^6 for the 7-foot 2-inch long model.

The tests were conducted at the Langley Pilotless Aircraft Research Station at Wallops Island, Va.

SYMBOLS

A	acceleration, ft/sec ²
C _D	drag coefficient, D/qS
c _f	local skin-friction coefficient
C _N	normal-force coefficient, Normal force/qS
C _{N_α}	rate of change of normal-force coefficient with α , $\frac{dC_N}{d\alpha}$
C _p	pressure coefficient, $\frac{P - P_\infty}{q_\infty}$
c _p	specific heat of air at constant pressure, Btu/lb-°F
c _w	specific heat of wall material, Btu/lb-°F
- D	drag, lb
D _{cyl}	cylinder diameter, ft
g	gravitational constant, 32.2 ft/sec ²
h	local aerodynamic heat-transfer coefficient, Btu/(sq ft)(sec)(°F)
k	thermal conductivity of air, Btu-ft/(sq ft)(sec)(°F)

~~CONFIDENTIAL~~

K_w	thermal conductivity of model skin material, Btu-ft/(sq ft)(sec)(°F)
M	Mach number
N_{Pr}	Prandtl number, $\frac{c_p \mu_g}{k}$
N_{St}	local Stanton number, $\frac{h}{c_{p,l} \rho_l V_l g}$
P	static pressure, lb/sq ft
q	dynamic pressure, lb/sq ft
R_{tr}	local Reynolds number at transition
R_l	local Reynolds number, $\frac{\rho_l V_l x}{\mu_l}$
r	radius, ft
S	cylinder cross-sectional area, sq ft
T	temperature, °R (unless otherwise noted)
t	time, sec
V	velocity, ft/sec
x	distance along body, ft (unless otherwise noted)
W	weight, lb
α	angle of attack, deg
ψ	radial angle between plane of angle of attack and line of thermocouples on body (see fig. 10(b))
σ	Stefan-Boltzman constant, 4.8×10^{-13} Btu/(sq ft)(sec)(°R ⁴)
ϵ	emissivity
ρ	density of air, slugs/cu ft
ρ_w	density of wall material, lb/cu ft

τ thickness of wall, ft (unless otherwise noted)
 η_r recovery factor
 μ viscosity of air, slugs/ft-sec

Subscripts:

aw adiabatic wall
i inner body
l local conditions just outside the boundary layer
t stagnation
w skin
 ∞ undisturbed free stream ahead of model

MODEL AND TESTS

Model Configuration

The general configuration of the model is shown in figure 1(a), and pertinent dimensions are given in figure 1(b). The conical nose had a total angle of 15° and was 31 inches long. The cylindrical section was 8.5 inches in diameter and 35 inches long. The flare skirt which provided aerodynamic stability had a 10° half-angle and a base diameter of 15.55 inches. Total length of the model was 86 inches.

The model skin was constructed from Inconel sheet about 0.03 inch thick. (See table I.) The tip of the nose was machined from solid Inconel, hollowed out, and welded to the spun Inconel nose skin at station $5\frac{1}{2}$. The point was rounded off with a radius of about 0.01 inch.

A threaded joint at the base of the nose cone allowed the nose skin to be removed for access to the telemeter, which was carried within the nose section. The flare skirt was welded to the cylinder, and a stiffening ring of 0.03-inch-thick steel was riveted inside the skin at the junction. Further stiffening of the flare skirt was provided by a balsa-wood core. Two channels, $1/4$ inch high by $3/4$ inch wide, formed from 0.03-inch-thick Inconel, were welded along opposite sides of the cylindrical section to provide conduits for instrumentation wires.

The entire model skin was carefully polished. After polishing, the nose cone skin was oxidized by heating for 9 minutes in an oven at 1,950° to 2,000° F. This was done so that the oxidation condition of the skin, which influences the emissivity, would not be in question at the high temperatures expected during the flight. The cylinder-flare assembly could not be oxidized because the available furnace was not large enough to accommodate it.

Surface roughness measurements made with a Physicist's Research Co. Profilometer were as follows: on the oxidized nose cone, 8 to 15 rms microinches, and on the cylinder and flare sections, 6 to 10 rms microinches. However, subsequent to the test, sample roughness measurements made with the profilometer on polished, unoxidized Inconel were checked optically with a fringe-type interference microscope. The average roughness measured optically was about 3 or 4 times the values read with the profilometer. Readings could not be obtained with the interference microscope on oxidized Inconel. It appears that the surface roughness of the cylinder and flare skins probably was about 30 to 40 microinches.

Instrumentation

Twenty-three thermocouples were installed along the model skin: 12 on the nose cone, 5 on the cylinder, and 6 on the flare skirt. The thermocouple stations are indicated in the drawing of the model (fig. 1(b)). They were in a longitudinal line which was 90° circumferentially from the channels on the cylindrical section. The thermocouples were No. 30 chromel-alumel wires, with each wire individually spot-welded to the inner surface of the skin.

During flight the output of the thermocouples and three standard voltages were commutated at a rate such that each of these items was recorded six times per second. The three standard voltages, supplied by a mercury cell and voltage-dividing network, were chosen equivalent to the lowest temperature, the midrange temperature, and the highest temperature that the skin thermocouples were expected to reach. Commutation and transmission of these known voltages along with the voltage readings of the thermocouples provided an "in-flight" calibration of the thermocouple telemeter and recording system.

Measurements of thrust, drag, and normal and transverse accelerations were also telemetered. The accelerometers and the telemeter were carried in the nose section of the model. They were protected from the high temperatures reached by the skin during flight by a highly polished Inconel radiation shield inside, but not touching, the nose skin. A thermocouple was also installed on the radiation shield.

~~CONFIDENTIAL~~

Propulsion and Test Technique

The propulsion system consisted of four stages of rocket motors. The first and second stages were each an M5 JATO, the third stage consisted of a bundle of three ABL Deacon motors carried within a cylindrical skin, and the fourth stage was a T40 motor carried within the cylindrical portion of the model. A photograph of the model and boosters on the launcher is shown in figure 1(c).

The firing times for the various stages were chosen to obtain the maximum Mach number possible without exceeding allowable skin temperatures. Premature separation of the later stages was prevented by locking devices between the second, third, and fourth stages. The motors were fired by delay squibs ignited at launching. Disengagement of the lock mechanism between the second and third stages was also accomplished by a delay squib, while the lock between the third and fourth stages was disengaged by the ignition blast of the fourth-stage motor.

The model was launched at an elevation angle of 70° . The test sequence was as planned until the time for ignition of the fourth-stage motor. Blast from the ignitor charge in the motor separated the model from the third stage satisfactorily, but the propellant grain did not ignite, and the model coasted upwards with decreasing Mach number instead of accelerating to a Mach number of 9 as intended. After separation an angle of attack occurred which had increased to about 9° when the range limit of Doppler radar was reached.

Time histories of free-stream Mach number and Reynolds number per foot are shown in figure 2(a) and altitude and free-stream static temperature are shown in figure 2(b). Velocity data were obtained by means of CW Doppler radar, and altitude and flight-path data were measured by an NACA modified SCR-584 tracking radar. Atmospheric conditions and wind directions and velocities were measured by radiosondes launched near the time of flight and tracked by a Rawin set AN/GMD-1A.

DATA REDUCTION

Heat Transfer

The time rate of change of heat stored in the model skin, per unit area, is

$$\rho_w c_w T \frac{dT_w}{dt} \quad (1)$$

and can be equated to the sum of the heat-flow terms, of which the most important are aerodynamic heating:

$$h(T_{aw} - T_w) \quad (2)$$

external radiation:

$$-\sigma \epsilon_w T_w^4 \quad (3)$$

internal radiation:

$$-\sigma(T_w^4 - T_1^4) / \left(\frac{r_w}{r_1} \frac{1}{\epsilon_1} + \frac{1}{\epsilon_w} - 1 \right) \quad (4)$$

conduction on nose cone:

$$K_w \tau \left(\frac{d^2 T_w}{dx^2} + \frac{1}{x} \frac{dT_w}{dx} \right) \quad (5)$$

and conduction on cylinder:

$$K_w \tau \frac{d^2 T_w}{dx^2} \quad (6)$$

The internal-radiation term is for coaxial cylinders (ref. 2) but was sufficiently accurate for the nose cone as well as the cylinder since its influence on the determination of h was a maximum of 10 percent and generally was less than 1 percent. It was disregarded for the flare stations since the flare was backed by balsa wood.

Solar radiation was neglected since estimates showed that its maximum effect on the determination of h was less than 2 percent. The conduction terms (eqs. 5 and 6) were neglected since their effects were less than 1 percent at all cylinder and flare stations other than the two closest to the cylinder-flare juncture. At these two stations and at the cone stations the effect was probably larger, particularly at times when aerodynamic heating was small, but the term could not be evaluated because the irregular temperature gradients and limited number of measurement points made the determination of $d^2 T_w / dx^2$ completely unreliable.

The expression used to determine the heat-transfer coefficient was then

$$h = \frac{\rho_w c_w \tau \frac{dT_w}{dt} + \sigma \epsilon_w T_w^4 + \frac{\sigma (T_w^4 - T_1^4)}{\frac{r_w}{r_1} \frac{1}{\epsilon_1} + \frac{1}{\epsilon_w} - 1}}{T_{aw} - T_w} \quad (7)$$

and local Stanton numbers were computed from

$$N_{St} = \frac{h}{c_p \rho_l V_l g} \quad (8)$$

Values of h were determined for each station for several times during the test by using the measured skin temperatures and graphically determined values of dT_w/dt . The skin thicknesses τ were measured and are given in table I. The density of Inconel ρ_w was a known constant of 518 pounds per cubic foot. The specific heat of Inconel c_w and the emissivity ϵ for polished and oxidized Inconel are shown as functions of temperature in figure 3 as obtained from reference 3. The polished radiation shield, which was the inner body for the nose cone, had a constant value of ϵ_1 of 0.28 since its temperature was between 70° F and 110° F during the test. The oxidized steel case of the rocket motor, which was the inner body for the cylinder, was assumed to have a value ϵ_1 of 0.7 and a temperature T_1 of 70° F.

Adiabatic-wall temperature was computed from

$$T_{aw} = \eta_r (T_t - T_l) + T_l \quad (9)$$

by using both theoretical and experimental values of η_r . For theoretical values of η_r , the usual $N_{Pr}^{1/3}$ for turbulent flow and $N_{Pr}^{1/2}$ for laminar flow were used, with N_{Pr} evaluated at wall temperature. Determination of the experimental values of η_r is explained in the next section. Stagnation temperature T_t was calculated from flight conditions with the variation of c_p with temperature being considered. Values of the local flow condition T_l , ρ_l , and V_l were determined as explained in the appendix.

Experimental Recovery Factors

At times when the aerodynamic heat transfer was zero, T_W was equal to T_{aw} , and equation (7) reduces to

$$\rho_W C_W T \frac{dT_W}{dt} = -\sigma \epsilon_W T_W^4 - \frac{\sigma (T_W^4 - T_i^4)}{\frac{r_W}{r_i} \frac{1}{\epsilon_i} + \frac{1}{\epsilon_W} - 1} \quad (10)$$

The times at which this equality existed were determined, and experimental values of η_r were computed from

$$\eta_r = \frac{T_{aw} - T_l}{T_t - T_l} \quad (11)$$

by substituting the measured values of T_W for T_{aw} .

Angle of Attack and C_D

The resultant acceleration perpendicular to the longitudinal axis and its radial orientation were found from the telemetered normal and transverse accelerations. Approximate angles of attack were then computed from the equation

$$\alpha = \frac{W}{g} \frac{A_{\text{resultant}}}{C_{N_\alpha} q S} \times 57.3 \quad (12)$$

Estimated values of $C_{N_\alpha} (\alpha = 0)$, which varied from 0.13 per radian at $M = 3$ to 0.115 per radian at $M = 7$, were used in equation (12). Angle of attack was determined for the present model at times after separation from the third-stage booster and for the model of reference 1 during coast after peak Mach number when drag measurements herein reported were obtained.

Drag coefficients were reduced from the accelerometer data of the present test and the test of reference 1 by the equation

$$C_D = \frac{W}{g q S} (A_{\text{longitudinal}} + A_{\text{resultant}} \sin \alpha) \quad (13)$$

Drag coefficients were also obtained in the present test by differentiating Doppler velocity data and using these acceleration values in the equation

$$C_D = \frac{W}{gqS} (A_{\text{Doppler}} - g \sin \theta) \quad (14)$$

where θ is the angle of the flight path with the horizon.

RESULTS AND DISCUSSION

Temperature Measurements and Heating Rates

The temperatures measured at the 12 nose-cone stations are shown in figures 4(a) to 4(c), the 5 cylinder stations in figure 4(d), and the 6 flare stations in figure 4(e). The temperatures on the cylinder, and, likewise, those on the flare, were within 16° F of each other at times prior to about 20 seconds and are indicated by a single line in figures 4(d) and 4(e). The values for each of these stations are listed in table II for times when N_{gt} data were compiled. Temperatures for the nose-cone stations are not tabulated since they can be read accurately from the curves of figures 4(a) to 4(c).

The temperatures at all stations increased most rapidly near 8 seconds when the altitude was about 10,000 feet and the Mach number was 3. The maximum rate was 177° per second at station 6.5. At 21 seconds the Mach number was 4, but the higher altitude of 41,000 feet caused the heating rates to be slightly less than at the earlier time. Near 22 seconds an abrupt reduction in rate of rise of skin temperature on the cone and forward part of the cylinder suggests that the boundary layer changed from turbulent to laminar as the Mach number increased to its maximum value of 4.7. This is confirmed by the Stanton numbers presented later.

The distribution of actual heat-transfer rate along the body is shown in figure 5 for time 22 seconds. Transition occurred about halfway back on the nose cone at this time, and caused a large variation in heat transfer along the nose. At 22 seconds the heating rates on the flare skirt were approximately the same as on the rear part of the nose. They were also similar at all times during the test except when the flow was laminar on the entire nose.

The heating rates on the cylinder were roughly one-half those on the flare as the Mach number increased from 2 to 4.70 during the time period from 16 to 22 seconds.

~~CONFIDENTIAL~~

Figure 5 shows approximately the highest rates measured during the test, except for locations ahead of station 25. Stations along the forward part of the nose attained maximum values of 20 to 25 Btu/(sec)(sq ft) at about 8 seconds. At 16.0 seconds when the skin was being cooled by the boundary layer, the rates were -2 to -3 Btu/(sec)(sq ft) on the cone and flare and about -1.5 Btu/(sec)(sq ft) on the cylinder.

Local Flow Parameters

Local flow conditions for each station were determined as described in the appendix. Figure 6 shows time histories of M_l , T_l , and of R_l based on length from the nose tip to the measurement station. On the cone, values of M_l and T_l are the same for each station. For the cylinder and for the flare, values of M_l and T_l are shown for the most forward and most rearward stations. Values of R_l based on length from the nose tip to the measurement station are likewise plotted for the most forward and most rearward stations on the three sections of the body. Linear interpolation gives accuracy within 2 or 3 percent for M_l , T_l , and R_l on the cylinder and flare. The exact values are given in tables III to V.

Time histories of the ratio T_w/T_l are shown in figure 7. The spread of this ratio for each section of the body is shown; values for each station can be obtained from the plotted or tabulated values of T_w and T_l .

Heat Transfer With Theoretical η_r

The experimental heat-transfer data obtained by using theoretical recovery factors are plotted in figure 8 as distributions of Ng_t along the body for a succession of times throughout the test. The data for typical stations on the nose cone, the cylinder, and the flare are plotted against time in figure 9.

Curves of theoretical Ng_t are also shown in figures 8 and 9 for comparison with the data. The laminar values for the nose cone were obtained from the flat-plate theory of reference 4 by using the local flow conditions and multiplying by the usual cone correction factor, $\sqrt{3}$. Theoretical turbulent values for the cone, cylinder, and flare were determined from local skin-friction coefficients by using the relation $Ng_t = 0.6c_f$ (see refs. 5 and 6). The values of c_f at local flow conditions were obtained from Van Driest's flat-plate theory as presented

CONFIDENTIAL

in charts in reference 7. The local Reynolds numbers used with the theory were based on one-half cone length plus cylinder length plus one-half flare length from the nose tip to the measurement station. For the cone stations the Reynolds numbers were thus one-half the values of R_L given in figure 6 and table V, in accordance with the theory of reference 8 for turbulent flow from the nose tip. For the cylinder stations the Reynolds numbers were equal to R_L times the factor $(x - 15.5)/x$ and for the flare they were equal to R_L times the factor $(x + 35)/2x$ where x is the station in inches.

The experimental N_{St} data in the plots of figure 8 are similar in trend along the body to the turbulent theory although the agreement in magnitude is not generally close at times prior to 20 seconds. For the cone stations, the poor agreement with the turbulent theory is unexpected since experimental data on the similar but unoxidized nose cone of reference 1 agreed closely with the theory.

Part of the scatter in the data shown in figures 8 and 9 for times from about 10 to 20 seconds can be attributed to the fact that the heating rates were relatively low between these times. Near 12 seconds and 19 seconds, T_w becomes equal to T_{aw} computed from theoretical recovery factors, as indicated in figure 9, and between these times the skin was being cooled relatively slowly. Since the accuracy of h as determined from equation (7) deteriorates as T_w approaches T_{aw} , more scatter would be expected in the N_{St} data at times from about 10 to 20 seconds than at earlier or later times. This is particularly shown in the time-history plots of figure 9 by the divergence in the N_{St} data as the condition $T_w = T_{aw}$ is approached. In the present case the divergence is toward a lower value of N_{St} when T_w is less than T_{aw} , toward a higher value of N_{St} when T_w is higher than T_{aw} and would have been reduced if the values of T_{aw} had been lower; that is, if the recovery factors had been lower.

The accuracy of the N_{St} data should be best for the time period 21 to 23 seconds (figs. 8(e) and 8(f)) because of the high heating potential $T_{aw} - T_w$ associated with this high Mach number part of the test. The data show that laminar flow occurred first at the forward nose station and spread back over the nose and body at times near maximum Mach number. Transition Reynolds numbers are presented in a subsequent section.

The plots for times 21 to 23 seconds also indicate the following points: The laminar data on the nose cone were in fair agreement with

laminar theory, as was the case in reference 1 for the similar but unoxidized nose. The turbulent data on the cone were in fair agreement with the theory for turbulent flow from the nose tip. On the cylinder, the turbulent data for stations not closely behind transition were somewhat lower than the turbulent theory shown. (Basing the theory for the cylinder on length from the nose tip rather than on one-half cone length plus length along the cylinder, does not appreciably improve the agreement, since this lowers the theory by less than 10 percent at the front of the cylinder and by less than 5 percent at the rear.) The level of the turbulent data on the cylinder was highest close behind transition, as would be expected, but did not exceed the theory even when transition was on the cylinder. On the flare, the data were in fair agreement with the theory except at 23 seconds when transition was located on the cylinder.

Reference 9 reports heat-transfer measurements on a 10° flare preceded by an ogive-cylinder body of slightly higher fineness ratio than the present body. The flare was 1.73 cylinder diameters long. In that test, with transition on the cylinder, the heat transfer on the rearward half of the flare agreed well with flat-plate turbulent theory based on length from the start of the flare. This theory for the flare is included in figure 8(f). It is considerably higher than most of the present flare measurements except when transition was located on the cylinder.

At times after 23 seconds, figure 8(g) shows that the general level of the heat-transfer data increased markedly. This increase is attributed to angle-of-attack conditions which commenced when the model separated from the third-stage booster at 23 seconds. The angle of attack, determined as indicated in the section entitled "Data Reduction," increased almost linearly with time as shown in figure 10(a). The orientation of the line of thermocouples with the plane of the angle of attack, as determined from the normal and transverse accelerometer readings, varied as shown in figure 10(b).

As the angle of attack increased, the zero angle-of-attack values of the local flow parameters $c_p, \rho_l V_l$ which were used to convert experimental h to Ng_t doubtless become less accurate for all stations. Although corrections for angle of attack were not attempted for the cylinder and flare stations, values of $(c_p, \rho_l V_l)$ at the nose-cone stations were computed for the conditions of figure 10 by using second-order yawed cone theory (refs. 10 to 13). These values modified the experimental and theoretical data only slightly at times 24 and 25 seconds. At 26 seconds the experimental data were lowered by about 30 percent as shown in figure 8(g), while the effect on the theoretical data was to raise the turbulent values by 5 percent and lower the laminar values by 10 percent. The corrections do not improve the agreement

between experiment and theory. Probably the length used in determining local Reynolds number is invalid for the angle-of-attack conditions because of crossflow on the cone. It may be noted, however, that, at the angle of attack of 5° , the measured heat transfer on the flare was 50 percent higher than that predicted by the turbulent theory for zero angle of attack. At an angle of attack of 9° the measured values were more than double those predicted by theory for zero angle of attack, although some of the increase may be due to the location of transition which appears to have been near the rear of the cylinder.

Experimental Recovery Factors

The experimental recovery factors which were obtained at times of zero aerodynamic heating as described in the section entitled "Data Reduction" are shown in figure 11. Two sets of η_r values were obtained since the heating became zero twice at each station. Free-stream Mach numbers varied from 2.45 to 2.75, and table VI, which gives the times and corresponding local Mach numbers, shows that at each station M_1 was very similar for the two η_r evaluations.

Figure 11 shows that the two η_r values are different at most of the stations, and that all are lower than the theoretical values of $Pr^{1/3}$ (which were near 0.88) based on wall temperature. Agreement with the theoretical laminar value of $N_{Pr}^{1/2}$ is not to be expected since the N_{St} data of figures 8 and 9 indicate that the heat transfer all along the body was of turbulent level at times near η_r evaluations. The low level of the η_r data cannot be attributed to conduction, which was not considered in the heat balance as noted previously, since conduction could not affect all stations in the same direction. Figure 12 shows the temperature distributions along the body near the times of the two sets of η_r evaluations. Rough similarities exist between the recovery-factor distributions and the temperature distributions, but no way of correlating them has been found.

Heat Transfer With Experimental η_r

Although the unusually low values of η_r are unexplained, their use in place of the theoretical values of η_r results in a more regular variation of the N_{St} data over the changing conditions of the test. This is shown by figure 13 which presents the N_{St} data, based on experimental values of η_r for the same three stations shown in figure 9 where

the data were based on theoretical values of η_r . It is apparent that the previously noted divergence of the N_{St} data as T_w approaches T_{aw} , is greatly reduced, and that the data are in fair agreement with the turbulent theory at each of the three stations shown over the entire range of the flight conditions until near the end of the test when laminar-flow and angle-of-attack conditions occurred.

Use of the experimental recovery factors also results in more uniform distributions of N_{St} along the body, especially during the period of relatively low heat-transfer rates from 10 to 20 seconds. This can be seen by comparing the plots of figure 14, which show the N_{St} data based on experimental values of η_r for times 8, 16, and 20 to 23 seconds, with the plots for the same times in figures 8(b) and 8(d) to 8(f) where the data are based on theoretical values of η_r . The data for times 16.0 and 20.0 seconds show less scatter when based on experimental values of η_r , while the data for the times of stronger aerodynamic heating, 8 seconds and 21 to 23 seconds, are less affected by the change from theoretical to experimental values of η_r .

The heat-transfer results of the test, in general, indicate the following characteristics: For the nose cone, cylinder, and forward part of the flare, the data compare with the theories in essentially the same manner for either theoretical or experimental η_r : That is, on the nose cone the data show fair agreement with the laminar and turbulent cone theories; on the cylinder the data are somewhat lower than turbulent theory based on one-half cone length plus cylinder length; and on the flare, within about one cylinder diameter of the flare juncture, the data are in fair agreement with turbulent theory based on $1/2$ cone length, plus cylinder length, plus $1/2$ flare length. However, for the rearward part of the flare, the data based on theoretical η_r agreed fairly well with theory for the flare as stated above, while the data based on experimental η_r agree better with theory based on length from the start of the flare.

Prediction of Skin Temperatures

In order to determine the accuracy with which the theory would have predicted the measured skin temperatures, step-by-step computations were made for station 15.5 on the nose cone, station 55 on the cylinder, and station 75 on the flare by using the actual flight conditions and theoretical recovery factors. Comparisons of the measured and computed temperatures are shown in figure 15. The computations overestimated the temperatures on the nose and cylinder by about 50° F. On the flare, the

computations overestimated the measurements by a maximum of 400° F until after 23 seconds, when angle-of-attack conditions caused the flare temperatures to rise considerably faster than the values computed for zero angle of attack.

Transition

As noted previously, laminar flow first occurred at 20 seconds at the forward station on the nose cone, and spread back over the body as the Mach number increased from 3 to 4.7. Lower Reynolds numbers per foot had occurred earlier in the test, at times from 14 to 19 seconds, without indication of laminar flow at any measurement station. However, from 14 to 19 seconds the skin was hotter than the boundary layer, which would make laminar flow less likely than at 20 seconds.

Local transition Reynolds numbers based on length from the nose tip, determined from the N_{gt} plots of figure 8 are shown in figure 16(a) as a function of local Mach number. At the two highest Mach numbers the location of transition is not precise, and a range is shown for R_{tr} . Also shown in the figure are the transition Reynolds numbers obtained on the similar but polished and unoxidized nose cone of reference 1. The present values are much lower than those of reference 1 except at the maximum Mach number. Figure 16(b) shows the ratio of wall static temperature to local static temperature at the transition stations for the data of figure 16(a). The infinite stability boundary for two-dimensional disturbances, given in reference 14, is shown by the solid curve. At Mach numbers of 3.66, 4.12, and 4.25 the temperature conditions were more stabilizing for the present data than for the data of reference 1. Probably the values of R_{tr} are lower for the present test because of the rougher surface of the oxidized nose cone. The highest value of R_{tr} for the present test, 19×10^6 , which is in agreement with the cone data of reference 1 for a Mach number 4.7, occurred when transition was on the polished cylinder.

Drag.— Drag coefficients for the test configuration are shown in figure 17. The data points between Mach numbers 4.15 and 4.5 are from both telemetered accelerometer and Doppler radar measurements of the present test obtained after the model separated from the third-stage booster. The drag coefficient roughly doubled as the model went to an angle of attack of about 9°.

Drag accelerometer measurements, not previously reported, were obtained in the investigation of reference 1, wherein the external model configuration was identical to that of the present test. These are the data shown at Mach numbers between 6.9 and 7 in figure 17. The normal

~~CONFIDENTIAL~~

and transverse accelerometers carried in that model indicated that an angle of attack of 1° was reached during the coast after sustainer motor burnout while the drag measurements were being obtained. Failure of the telemeter signal ended the measurements at a Mach number of 6.9.

The solid curve, which is the total of the estimated C_D components shown by the broken curves, is in good agreement with the data near a Mach number of 7, and with the data for the lower angles of attack near a Mach number of 4.5.

CONCLUDING REMARKS

Measurements of aerodynamic heat transfer have been made during conditions of skin heating and skin cooling at 23 stations along the 7-foot 2-inch length of a cone-cylinder-flare model having a 15° total angle conical nose and a 10° half-angle flare skirt. Data were obtained at free-stream Mach numbers from 1.7 to 4.7. Local Reynolds numbers based on length from the nose tip to a measurement station covered the range from 2×10^6 to 138×10^6 .

Experimental recovery factors for turbulent boundary layer which were determined on two occasions during the test were unaccountably much lower than the theoretical value of Prandtl number $N_{Pr}^{1/3}$. Local Stanton numbers were determined from the skin-temperature measurements by using both theoretical and experimental recovery factors.

The data for the nose cone were in fair agreement with laminar and turbulent theories for cones. The turbulent measurements on the cylinder were generally somewhat lower than turbulent theory based on one-half the cone length plus length along the cylinder. Measurements along the flare within about one cylinder diameter of the start of the flare were in fair agreement with turbulent theory based on one-half the cone length plus cylinder length plus one-half the length along the flare. On the remainder of the flare, the measurements agreed best with theory based on length as just described or with theory based on length from the start of the flare, depending on whether the Stanton number data were determined by using theoretical or experimental recovery factors.

Local Reynolds numbers at the start of transition based on length from the nose tip and determined from the heat-transfer coefficients varied from 3×10^6 to 18×10^6 . These values were much lower than were previously obtained at fairly similar conditions on the smoother nose of a duplicate model.

During the later part of the test, the model pitched to an angle of attack of about 9° , and the turbulent heat transfer on the flare increased to more than twice the theoretical value for zero angle of attack.

Langley Aeronautical Laboratory,
National Advisory Committee for Aeronautics,
Langley Field, Va., September 25, 1957.

~~CONFIDENTIAL~~

APPENDIX

DETERMINATION OF LOCAL FLOW CONDITIONS

Nose Cone

The local flow parameters $\frac{M_L}{M_\infty}$, $\frac{V_L}{V_\infty}$, $\frac{\rho_L}{\rho_\infty}$, and $\frac{T_L}{T_\infty}$ for the nose cone stations were obtained from the cone tables given in reference 9.

Cylindrical Section

The static-pressure coefficients for the measurement stations on the cylindrical section were obtained from the data of reference 15 which presents a method of characteristics solutions of surface flow parameters for a family of cone-cylinder bodies at several Mach numbers. These static pressures presented as ratios of the local total pressure, which is the value behind the nose shock, gave the values of $\frac{M_L}{M_\infty}$ from which the other local flow parameters were computed by using isentropic flow relations.

Flare

Estimates of the static-pressure-coefficient distribution along the flare were based on the results of reference 16, which reports a wind-tunnel test on a cone-cylinder-flare model having a 20° total angle conical nose, a cylindrical section 2.96 diameters long, and a $9^\circ 36.3'$ half-angle flare. The model of the present test had a 15° total-angle conical nose, a cylindrical section 4.12 diameters long, and a 10° half-angle flare. The test of reference 16 was conducted at a Mach number of 1.90 and a Reynolds number of 3.2×10^6 based on body length. There was no indication of separated flow at the cylinder-flare juncture from the schlieren photographs or from the pressure measurements.

The measured pressure coefficients of reference 16 and the faired curve which was used for the flare pressure distribution in the present report are shown in figure 18 for $M = 1.9$. The measured values fall between the 10° cone and 10° wedge theories, and approached the cone theory at the rearward stations. The faired distribution along the non-dimensional flare length was applied for the present test at Mach numbers other than 1.9 by assuming that its relation to the cone and wedge theories was invariant with Mach number. The distributions obtained

thereby for Mach numbers 3.0 and 4.3 are shown in figure 18. Also shown at each Mach number are unpublished measurements for 10° flares recently obtained in rocket-powered flight tests. These data agree fairly well with the faired distribution for $M = 1.9$ and also substantiate its application to the higher Mach numbers, except at locations immediately behind the flare junction where the unpublished data are lower than the assumed distribution. This may be due to a small region of separated flow at the junction which could also have existed in the present test.

Total pressure along the flare was obtained by assuming a two-dimensional shock at the cylinder-flare juncture, with the Mach number ahead of the shock and static pressure ratio across the shock known from the values on the end of the cylinder and on the forward part of the flare. The static-pressure distribution and the total pressure gave the values of $\frac{M_1}{M_\infty}$ along the flare from which the other flow parameters were computed.

REFERENCES

1. Rumsey, Charles B., and Lee, Dorothy B.: Measurements of Aerodynamic Heat Transfer and Boundary-Layer Transition on a 15° Cone in Free Flight at Supersonic Mach Numbers Up to 5.2. NACA RM L56F26, 1956.
2. Schmidt, Ernst: Thermodynamics. The Clarendon (Oxford), 1949.
3. Ginnings, Defoe C., and Thomas, Eugenia: The Electrical Resistance and Total Radiant Emittance of Inconel in the Range 0° to 1000° C. NBS Rep. 4111 (NACA Contract S54-52), Nat. Bur. of Standards, May 1955.
4. Van Driest, E. R.: Investigation of Laminar Boundary Layer in Compressible Fluids Using the Crocco Method. NACA TN 2597, 1952.
5. Rubesin, Morris W.: A Modified Reynolds Analogy for the Compressible Turbulent Boundary Layer on a Flat Plate. NACA TN 2917, 1953.
6. Seiff, Alvin: Examination of the Existing Data on the Heat Transfer of Turbulent Boundary Layers at Supersonic Speeds From the Point of View of Reynolds Analogy. NACA TN 3284, 1954.
7. Lee, Dorothy B., and Faget, Maxime A.: Charts Adapted From Van Driest's Turbulent Flat-Plate Theory for Determining Values of Turbulent Aerodynamic Friction and Heat-Transfer Coefficients. NACA TN 3811, 1956.
8. Van Driest, E. R.: Turbulent Boundary Layer on a Cone in a Supersonic Flow at Zero Angle of Attack. Jour. Aero. Sci., vol. 19, no. 1. Jan. 1952, pp. 55-57, 72.
9. Becker, John V., and Korycinski, Peter F.: Heat Transfer and Pressure Distribution at a Mach Number of 6.8 on Bodies With Conical Flares and Extensive Flow Separation. NACA RM L56F22, 1956.
10. Staff of the Computing Section, Center of Analysis (Under Direction of Zdeněk Kopal): Tables of Supersonic Flow Around Cones. Tech. Rep. No. 1 (NOrd Contract No. 9169), M.I.T., 1947.
11. Staff of the Computing Section, Center of Analysis (Under Direction of Zdeněk Kopal): Tables of Supersonic Flow Around Yawing Cones. Tech. Rep. No. 3, M.I.T., 1947.
12. Staff of the Computing Section, Center of Analysis (Under Direction of Zdeněk Kopal): Tables of Supersonic Flow Around Cones of Large Yaw. Tech. Rep. No. 5, M.I.T., 1949.

~~CONFIDENTIAL~~

13. Roberts, Richard C., and Riley, James D.: A Guide to the Use of the M.I.T. Cone Tables. NAVORD Rep. 2606 (Aeroballistic Res. Rep. No. 123), U.S. Naval Ord. Lab. (White Oak, Md.), Apr. 1, 1953.
14. Van Driest, E. R.: Calculation of the Stability of the Laminar Boundary Layer in a Compressible Fluid on a Flat Plate With Heat Transfer. Jour. Aero. Sci., vol. 19, no. 12, Dec. 1952, pp. 801-812.
15. Clippinger, R. F., Giese, J. H., and Carter, W. C.: Tables of Supersonic Flows About Cone Cylinders. Part I: Surface Data. Rep. No. 729, Ballistic Res. Lab., Aberdeen Proving Ground, 1950.
16. Kelly, A. H., and Ross, F. W.: A Supersonic Body Profile Development Study. Report No. 4 - Twenty Degree Cone-Cylinder - Nine Degree Flare, Twenty Degree Cone-Cylinder - Five Degree Flare, Twenty Degree Cone - Four Degree Convergence - Five Degree Flare at Mach Number 1.90. Rep. No. UMM-58 (USAF Contract W-33-038-ac-14222), Aero. Res. Center, Univ. of Michigan, July 31, 1950.

TABLE I.- SKIN THICKNESSES

Cone		Cylinder		Flare	
Station, in.	Skin thickness, τ , in.	Station, in.	Skin thickness, τ , in.	Station, in.	Skin thickness, τ , in.
6.5	0.0308	35.0	0.0294	68.0	0.0291
8.0	.0304	45.0	.0294	70.0	.0286
9.5	.0316	55.0	.0289	72.0	.0296
11.0	.0308	64.0	.0263	75.0	.0282
12.5	.0305	65.0	.0260	80.0	.0287
14.0	.0309			85.0	.0315
15.5	.0303				
17.0	.0314				
19.0	.0316				
21.0	.0314				
25.0	.0301				
29.0	.0312				

TABLE II.- SKIN TEMPERATURES

t, sec	Skin temperatures, T_w , °F, on -										
	Cylinder					Flare					
	Station 35	Station 45	Station 55	Station 64	Station 65	Station 68	Station 70	Station 72	Station 75	Station 80	Station 85
6.0	97	95	97	95	96	102	102	100	104	103	102
7.0	141	142	146	144	148	168	163	161	158	160	157
7.5	178	181	183	182	184	223	216	212	208	212	207
8.0	223	227	229	226	235	289	283	276	282	278	277
8.5	270	276	280	274	286	361	357	354	356	351	349
9.0	311	318	323	318	328	413	413	411	412	407	402
9.5	345	347	352	352	360	446	446	446	448	443	437
10.0	369	368	373	377	382	467	468	470	470	466	458
11.0	394	396	400	402	405	484	487	489	489	486	476
12.0	405	407	409	410	413	482	485	487	488	485	475
14.0	401	401	404	404	407	455	459	456	459	456	450
15.0	398	393	395	395	398	437	440	437	440	437	432
16.0	383	382	385	383	386	417	419	419	421	418	413
18.0	359	357	361	358	360	375	377	382	380	382	374
18.5	352	352	354	351	354	366	369	372	371	373	366
19.0	348	348	349	346	349	359	363	362	363	365	360
20.0	347	348	350	346	348	363	363	365	365	367	366
21.0	366	372	375	370	372	406	411	411	412	409	407
21.5	388	392	395	394	398	447	459	460	463	459	453
22.0	419	420	422	422	425	507	523	526	530	522	516
23.0	451	458	473	476	478	609	635	637	635	626	613
24.0	482	494	518	520	524	680	710	709	705	690	674
25.0	517	535	553	553	559	738	760	759	754	738	722
26.0	532	552	571	572	583	787	798	799	793	776	759

TABLE III.- LOCAL MACH NUMBER

t, sec	Local Mach number M_L for -											
	Cone	Cylinder					Flare					
	All stations	Station 35	Station 45	Station 55	Station 64	Station 65	Station 68	Station 70	Station 72	Station 75	Station 80	Station 85
6.0	1.58	1.77	1.69	1.69	1.69	1.68	1.42	1.41	1.45	1.47	1.49	1.51
7.0	2.17	2.43	2.35	2.33	2.32	2.31	2.01	2.00	2.03	2.07	2.09	2.09
7.5	2.49	2.80	2.72	2.70	2.68	2.67	2.34	2.32	2.34	2.38	2.39	2.39
8.0	2.82	3.19	3.11	3.09	3.04	3.05	2.66	2.65	2.67	2.70	2.71	2.72
8.5	2.88	3.23	3.16	3.15	3.11	3.10	2.69	2.69	2.71	2.74	2.75	2.75
9.0	2.78	3.11	3.03	3.01	2.99	2.99	2.60	2.59	2.61	2.65	2.66	2.67
9.5	2.69	3.02	2.94	2.92	2.89	2.89	2.51	2.51	2.53	2.57	2.58	2.58
10.0	2.63	2.95	2.87	2.85	2.82	2.81	2.47	2.46	2.47	2.51	2.51	2.51
11.0	2.50	2.81	2.73	2.71	2.69	2.68	2.35	2.33	2.36	2.39	2.41	2.40
12.0	2.39	2.69	2.60	2.59	2.57	2.56	2.24	2.23	2.25	2.29	2.31	2.29
14.0	2.20	2.48	2.39	2.38	2.36	2.35	2.06	2.04	2.07	2.10	2.12	2.12
15.0	2.12	2.39	2.29	2.29	2.27	2.27	1.98	1.98	1.99	2.01	2.04	2.03
16.0	2.05	2.30	2.21	2.20	2.19	2.18	1.90	1.89	1.91	1.95	1.97	1.97
18.0	1.93	2.18	2.09	2.09	2.07	2.06	1.79	1.79	1.81	1.84	1.87	1.87
18.5	1.92	2.17	2.08	2.08	2.06	2.05	1.78	1.78	1.80	1.83	1.86	1.86
19.0	2.19	2.47	2.38	2.37	2.35	2.34	2.04	2.03	2.06	2.09	2.11	2.11
20.0	2.85	3.21	3.13	3.11	3.07	3.07	2.67	2.67	2.68	2.72	2.73	2.73
21.0	3.66	4.14	4.08	4.04	4.00	4.00	3.37	3.37	3.40	3.41	3.41	3.47
21.5	4.12	4.73	4.66	4.63	4.58	4.58	3.77	3.77	3.81	3.81	3.82	3.88
22.0	4.25	4.89	4.81	4.78	4.72	4.72	3.87	3.87	3.91	3.91	3.91	3.98
23.0	4.13	4.74	4.67	4.64	4.59	4.59	3.78	3.78	3.82	3.82	3.83	3.89
24.0	4.01	4.59	4.51	4.49	4.45	4.45	3.68	3.69	3.72	3.72	3.73	3.79
25.0	3.95	4.52	4.45	4.41	4.37	4.37	3.62	3.62	3.67	3.68	3.68	3.73
26.0	3.83	4.37	4.29	4.27	4.21	4.21	3.51	3.51	3.56	3.58	3.58	3.61

CONFIDENTIAL

CONFIDENTIAL

TABLE IV.- LOCAL TEMPERATURE

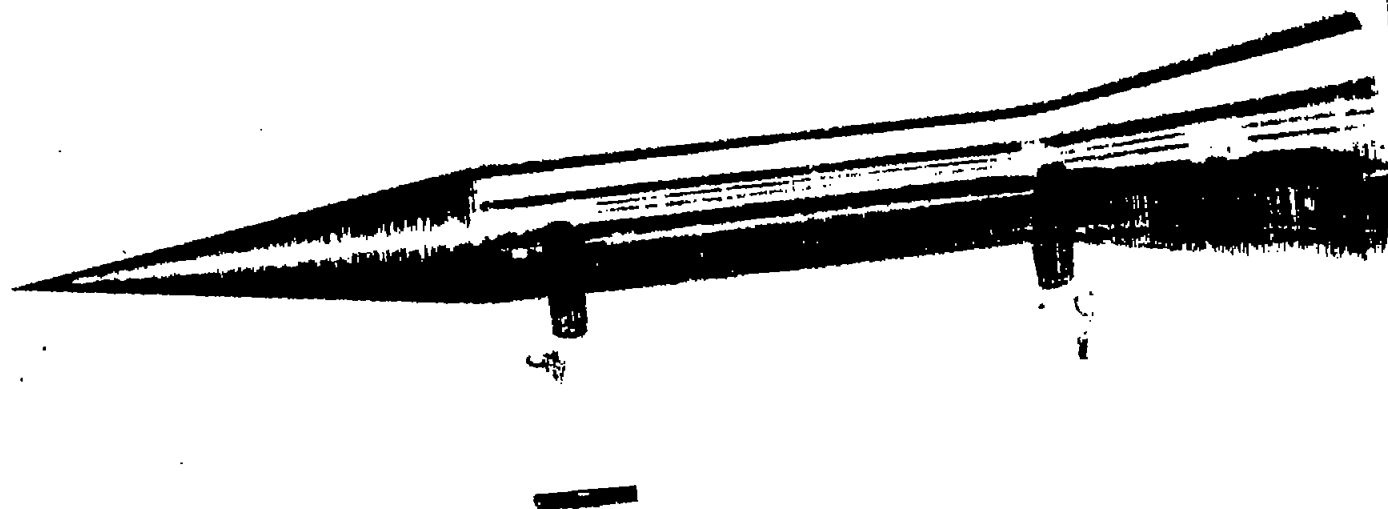
t, sec	Local temperature T_l , $^{\circ}\text{R}$, on -											
	Cone	Cylinder					Flare					
	All stations	Station 35	Station 45	Station 55	Station 64	Station 65	Station 68	Station 70	Station 72	Station 75	Station 80	Station 85
6.0	507	464	479	482	485	486	542	537	537	530	527	522
7.0	515	455	470	476	479	480	554	554	549	544	539	537
7.5	521	453	466	473	476	477	562	562	557	554	547	545
8.0	522	448	460	467	470	471	570	570	565	560	555	553
8.5	521	445	457	464	468	468	569	569	565	560	552	552
9.0	515	443	455	462	465	466	559	559	556	552	547	544
9.5	506	436	449	456	459	459	548	548	546	539	537	534
10.0	500	432	445	451	454	455	541	541	536	532	529	527
11.0	484	421	434	440	443	444	522	522	518	516	509	511
12.0	472	412	425	431	433	434	509	506	506	500	498	493
14.0	452	399	411	416	419	420	485	487	481	476	472	472
15.0	438	389	401	406	409	410	470	470	466	461	458	456
16.0	428	381	393	398	400	401	458	458	454	450	446	445
18.0	408	366	378	382	384	385	439	437	433	429	427	425
18.5	406	365	376	380	383	383	437	436	432	426	426	424
19.0	413	365	377	381	384	385	444	444	440	436	432	432
20.0	430	368	378	384	387	387	469	469	465	461	457	456
21.0	448	369	379	385	388	388	502	502	500	494	490	490
21.5	458	369	378	383	387	388	525	525	523	518	514	514
22.0	459	367	376	382	385	386	529	531	527	523	517	515
23.0	453	365	374	379	383	383	519	519	517	514	508	508
24.0	452	367	376	381	385	385	516	518	514	510	506	504
25.0	446	363	372	377	381	381	507	509	505	503	497	495
26.0	439	359	369	374	377	378	496	500	496	491	485	485

TABLE V.- LOCAL REYNOLDS NUMBERS

t, sec	Reynolds number R_1 per inch on cone	Reynolds number R_1 on -										
		Cylinder					Flare					
		Station 35	Station 45	Station 55	Station 64	Station 65	Station 68	Station 70	Station 72	Station 75	Station 80	Station 85
6.0	0.9×10^6	29.5×10^6	38.4×10^6	47.9×10^6	56.2×10^6	56.8×10^6	63.3×10^6	63.6×10^6	66.8×10^6	69.3×10^6	73.2×10^6	76.7×10^6
7.0	1.2	37.4	49.2	61.0	71.6	72.3	88.9	89.4	92.7	95.9	101.6	105.5
7.5	1.4	40.9	53.9	67.3	78.6	79.7	102.4	103.0	106.1	109.2	115.2	120.6
8.0	1.5	43.9	58.7	73.3	85.3	87.0	116.7	117.6	120.8	124.1	130.5	136.9
8.5	1.5	42.4	56.6	71.0	82.5	83.8	112.3	113.7	117.4	119.9	126.6	132.3
9.0	1.4	38.7	51.5	64.5	75.3	76.8	102.0	102.9	105.5	108.7	114.2	120.1
9.5	1.3	36.4	48.2	60.2	70.2	71.5	93.3	94.4	96.7	99.6	104.9	110.6
10.0	1.2	34.1	45.3	56.4	65.8	66.6	87.5	88.2	90.4	93.1	97.4	102.1
11.0	1.0	30.4	40.2	50.3	58.7	59.3	76.1	76.6	79.4	81.4	85.9	89.5
12.0	.9	26.9	35.4	44.3	51.7	52.2	66.2	66.4	68.6	71.0	73.3	77.8
14.0	.7	21.3	27.9	33.0	40.8	41.2	50.9	51.0	53.1	54.5	57.8	60.2
15.0	.6	19.3	25.2	31.6	36.8	37.4	45.7	46.2	47.4	48.7	51.7	53.4
16.0	.6	17.4	22.8	28.5	33.3	33.6	40.6	40.7	42.1	43.5	46.4	48.2
18.0	.5	14.6	19.0	23.9	27.9	28.1	33.3	33.8	35.0	36.1	38.4	40.1
18.5	.4	14.0	18.2	22.8	26.5	26.8	31.7	32.2	33.1	34.4	36.6	38.1
19.0	.5	15.0	19.6	24.5	28.6	28.8	35.5	35.7	37.1	38.2	40.2	42.1
20.0	.6	16.7	22.4	27.9	33.5	33.0	44.1	44.5	45.7	47.0	49.5	52.0
21.0	.7	18.1	24.2	30.3	35.4	36.2	52.2	52.7	54.1	55.6	58.1	61.8
21.5	.8	18.6	24.9	31.4	36.7	37.0	56.4	57.1	58.7	60.2	62.8	66.4
22.0	.7	17.4	23.4	29.4	34.4	34.7	53.5	53.9	55.7	57.1	59.5	63.1
23.0	.6	14.0	18.7	23.7	27.6	27.9	42.3	43.0	44.1	45.2	47.3	50.2
24.0	.5	11.1	14.8	18.7	21.9	22.1	33.3	33.7	34.7	35.5	37.2	39.5
25.0	.4	9.2	12.3	15.4	18.0	18.3	27.3	27.5	28.5	29.3	30.6	32.3
26.0	.3	7.6	10.1	12.8	14.8	15.0	22.1	22.3	23.1	23.7	24.9	26.1

TABLE VI.- TIMES AND CONDITIONS FOR EXPERIMENTAL
RECOVERY FACTOR EVALUATIONS

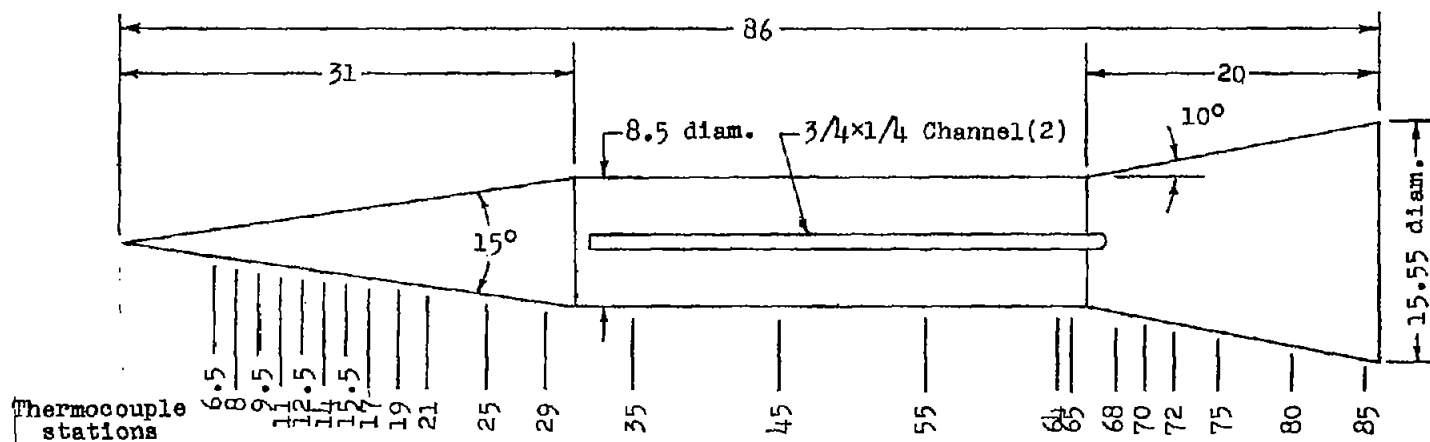
Station	First evaluation			Second evaluation		
	t, sec	M_L	η_r	t, sec	M_L	η_r
6.5	10.53	2.56	0.750	19.60	2.48	0.663
8.0	10.82	2.51	.747	19.33	2.41	.706
9.5	10.68	2.54	.781	19.23	2.37	.795
11.0	11.18	2.48	.795	19.25	2.36	.796
12.5	10.98	2.50	.792	19.28	2.36	.813
14.0	11.12	2.48	.833	19.50	2.49	.741
15.5	10.88	2.51	.738	19.23	2.35	.864
17.0	11.20	2.47	.693	19.21	2.34	.783
19.0	11.08	2.48	.743	19.34	2.41	.766
21.0	11.74	2.40	.786	19.30	2.38	.784
25.0	11.18	2.48	.684	19.24	2.36	.774
29.0	11.25	2.47	.731	19.25	2.36	.811
35.0	12.82	2.60	.852	19.62	2.89	.724
45.0	12.64	2.53	.849	19.39	2.62	.836
55.0	12.52	2.52	.826	19.45	2.66	.777
64.0	12.53	2.52	.827	19.48	2.66	.778
65.0	12.47	2.51	.832	19.49	2.67	.778
68.0	11.36	2.31	.793	19.41	2.28	.782
70.0	11.42	2.29	.812	19.43	2.29	.782
72.0	11.36	2.31	.808	19.46	2.33	.763
75.0	11.42	2.35	.800	19.52	2.39	.732
80.0	11.56	2.34	.816	19.46	2.37	.775
85.0	11.34	2.36	.788	19.42	2.38	.778



(a) Photograph of model.

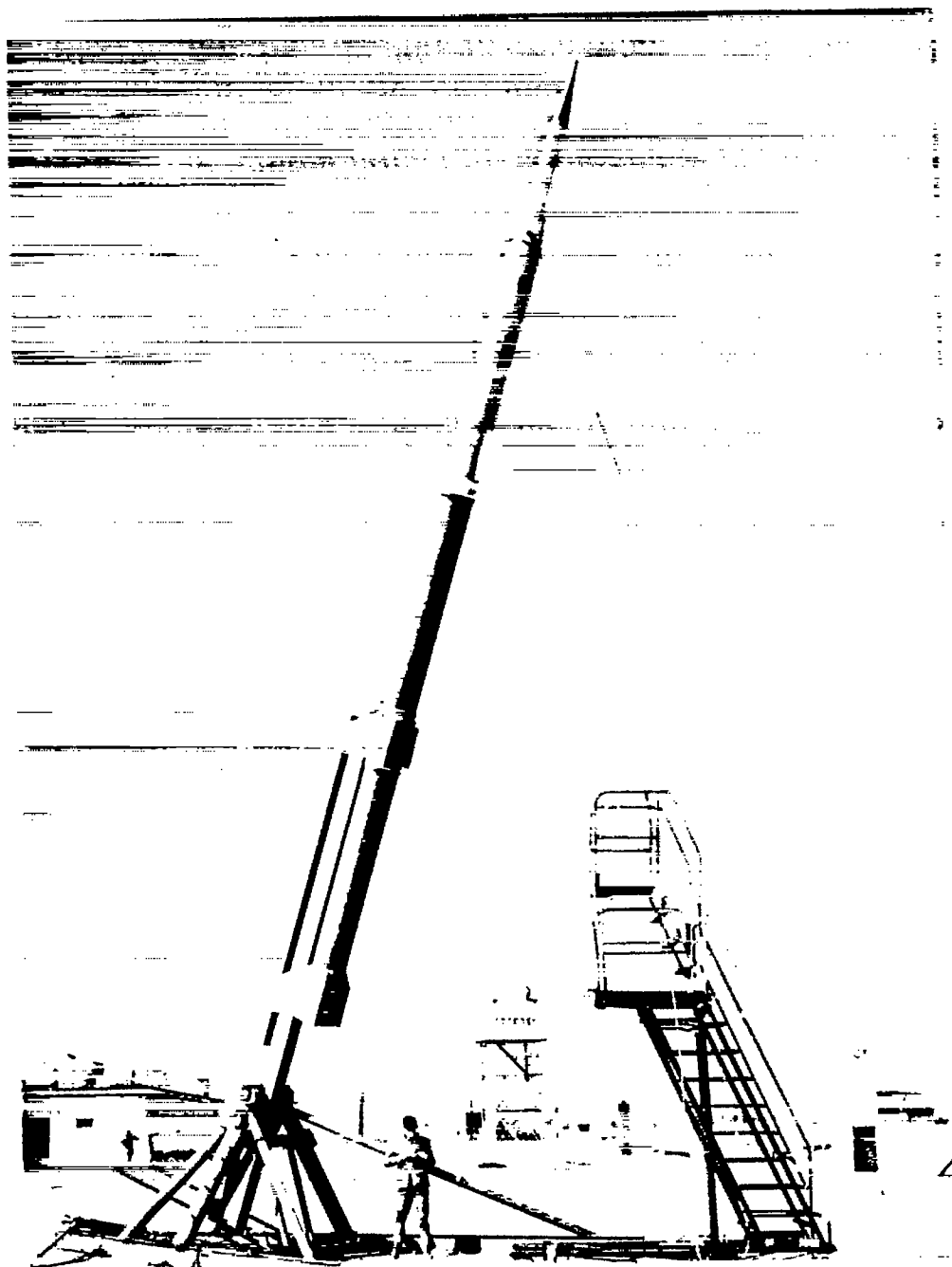
Figure 1.- Test configuration.

L-88812



(b) Model dimensions and thermocouple stations. Dimensions in inches.

Figure 1.- Continued.

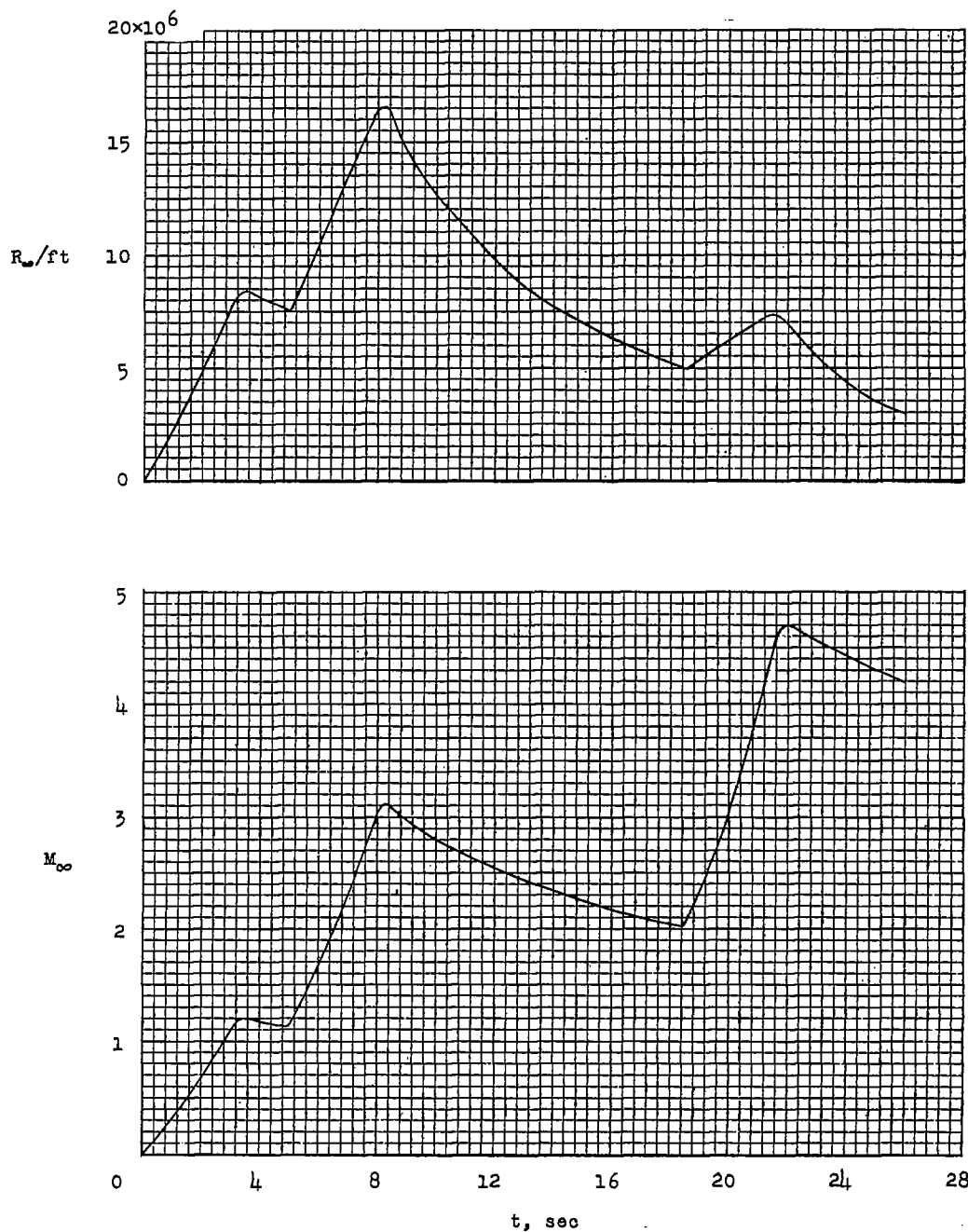
~~CONFIDENTIAL~~

(c) Model and boosters on launcher.

L-89108

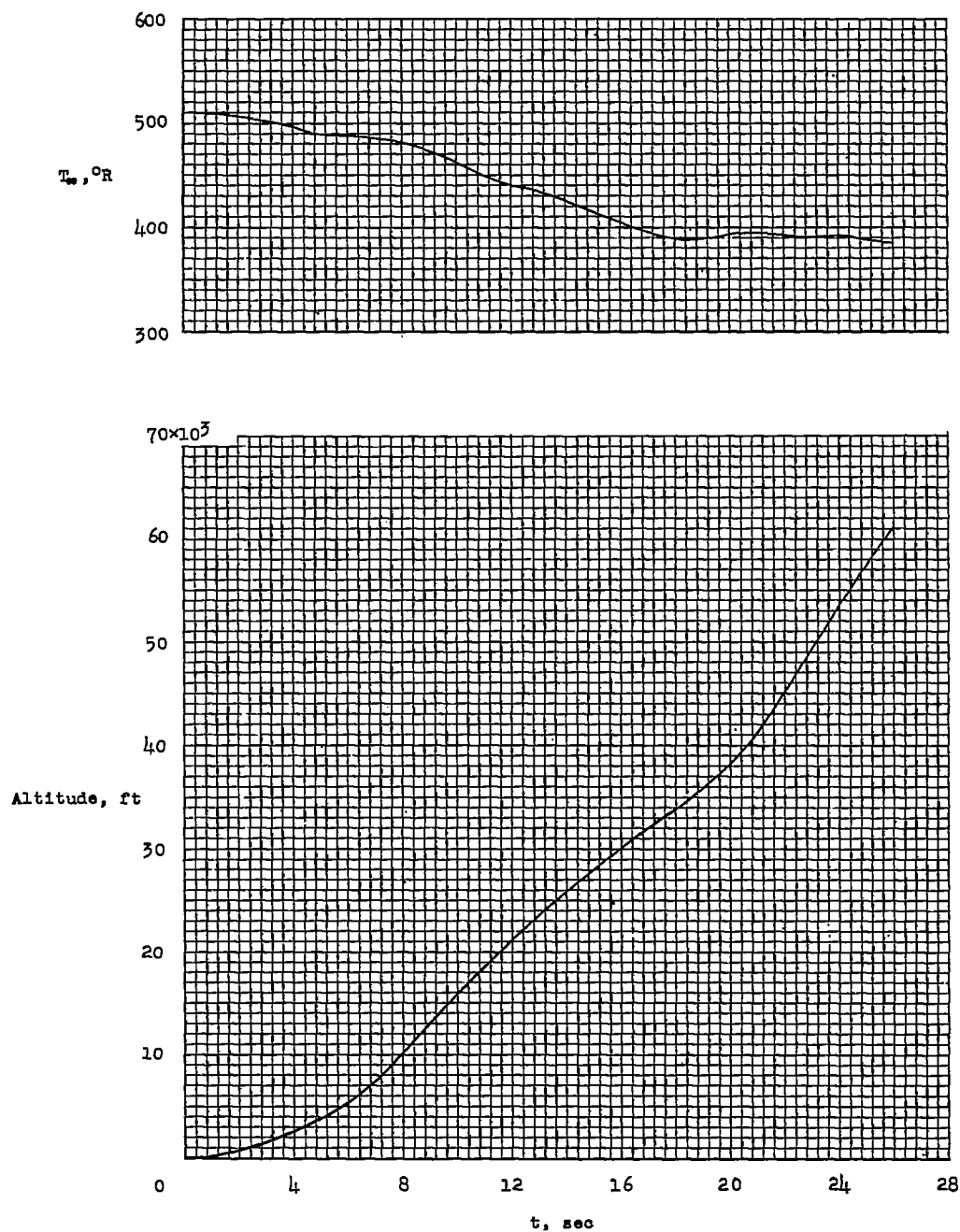
Figure 1.- Concluded.

~~CONFIDENTIAL~~



(a) Free-stream Reynolds number per foot and free-stream Mach number.

Figure 2.- Time histories of free-stream test conditions.



(b) Altitude and free-stream static temperature.

Figure 2.- Concluded.

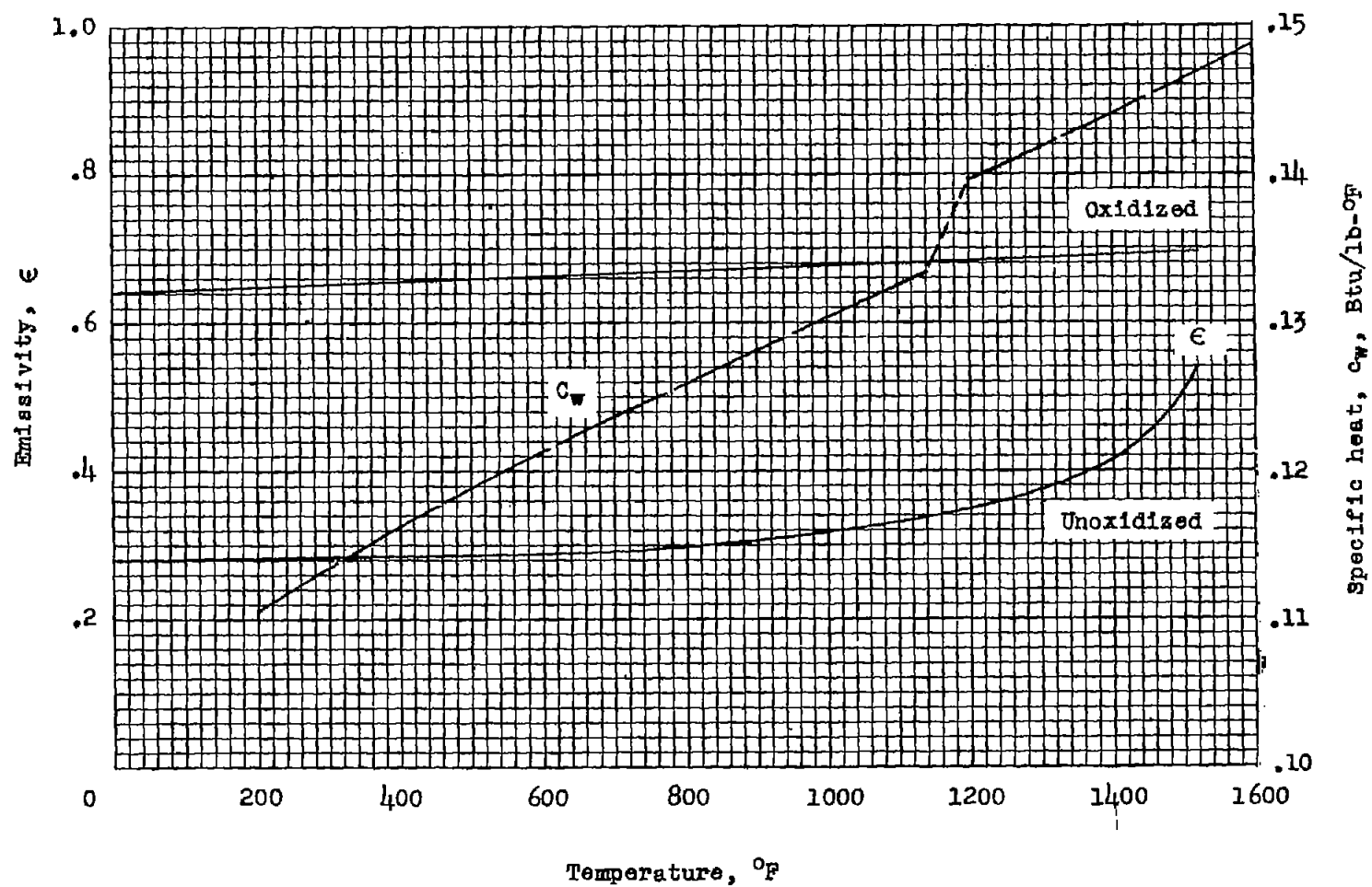
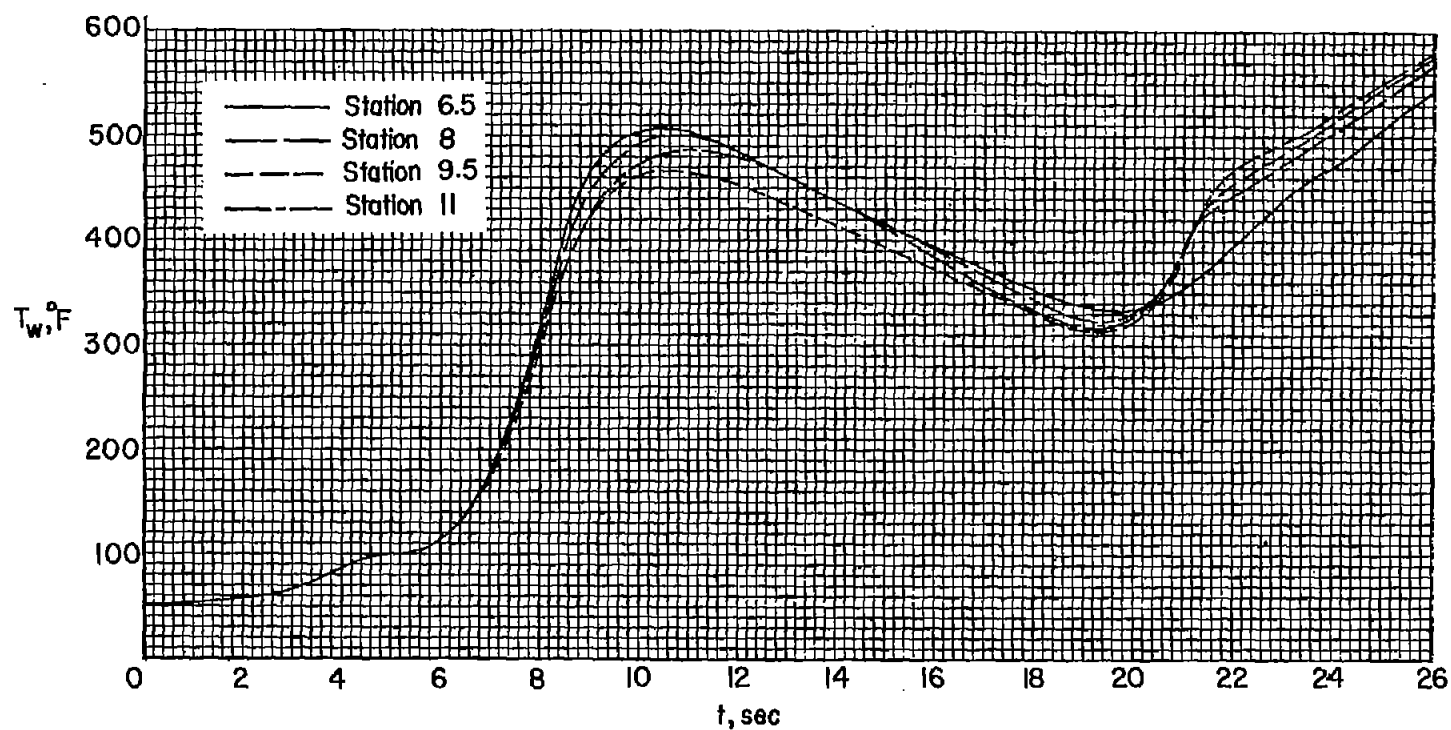
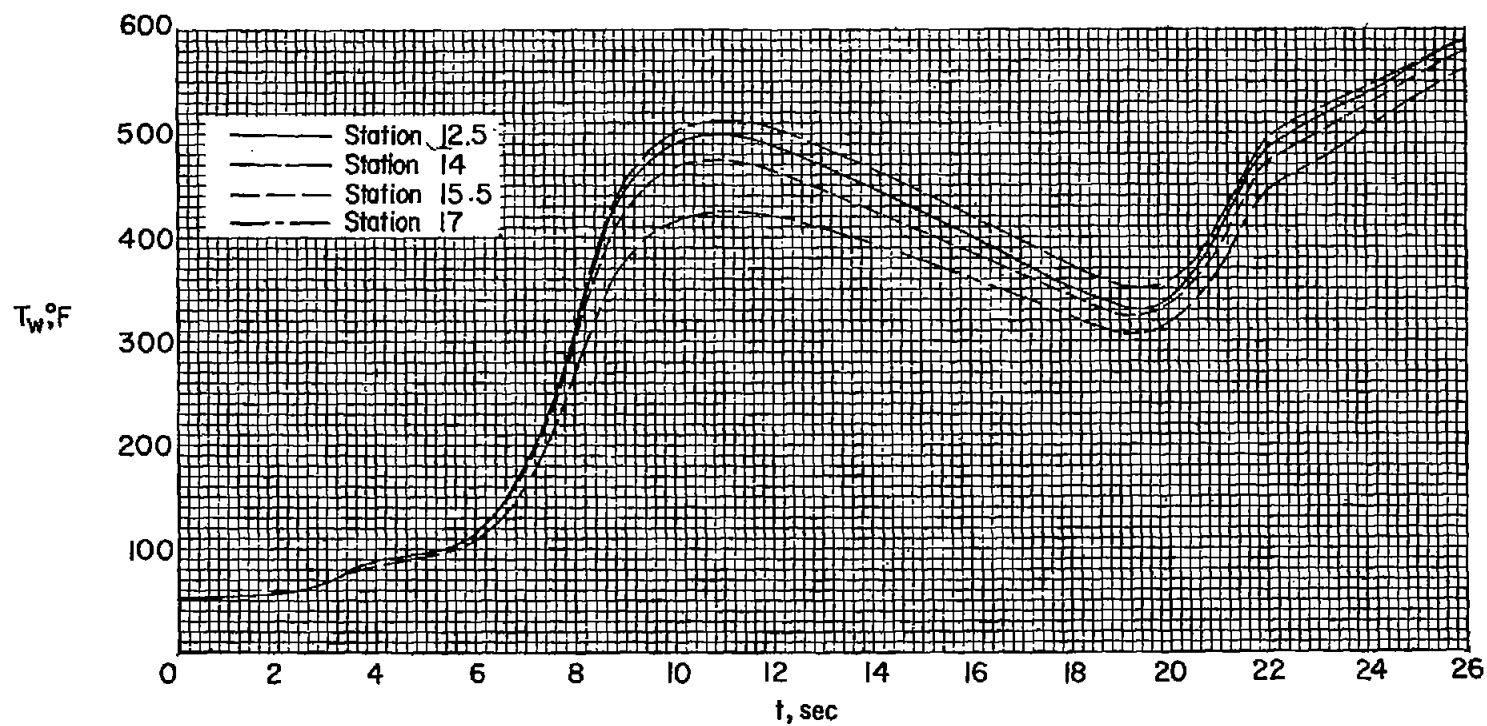


Figure 3.- Emissivity and specific heat of Inconel.



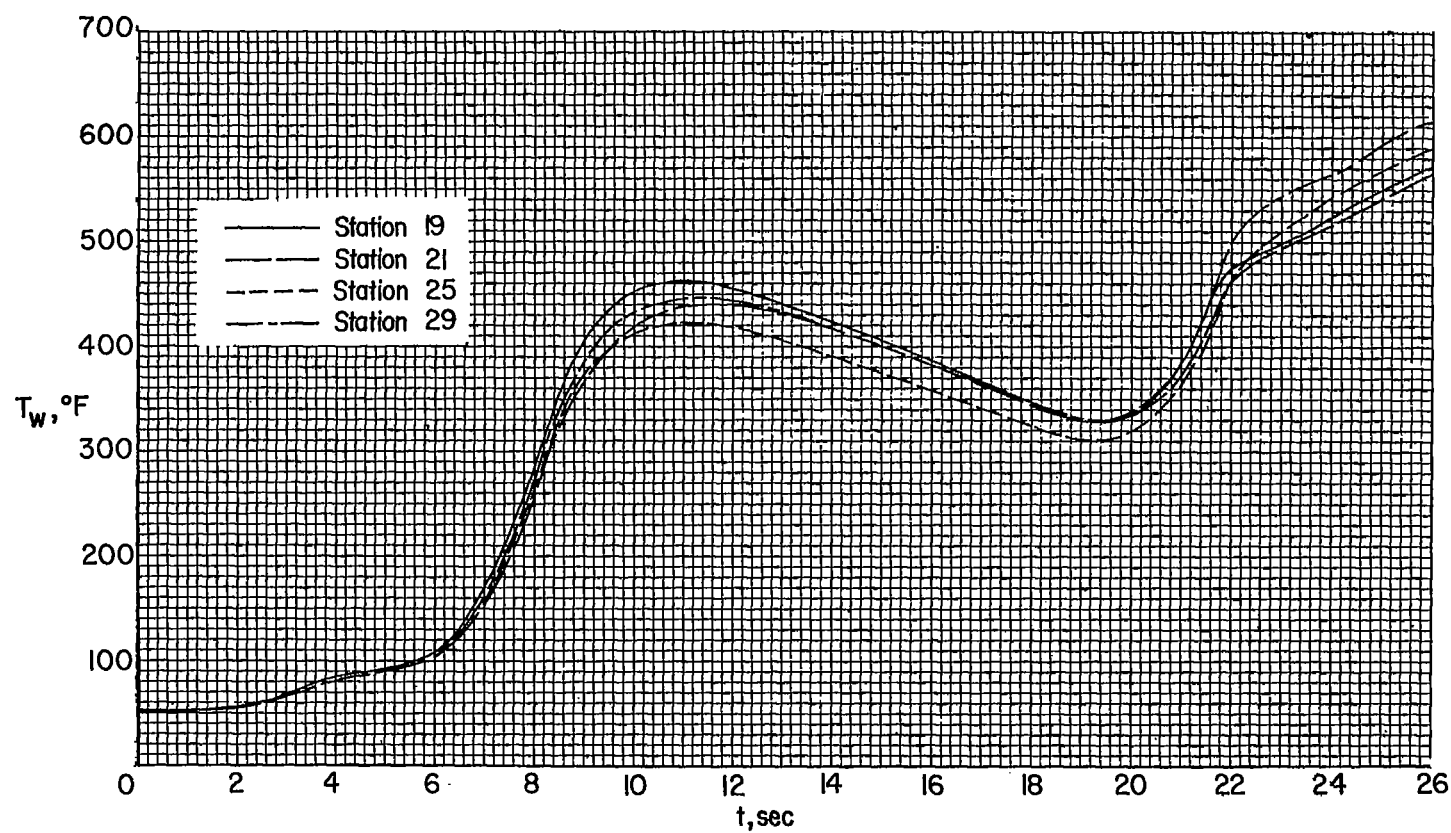
(a) Nose-cone stations 6.5, 8.0, 9.5, and 11.0.

Figure 4.- Measured skin temperatures.



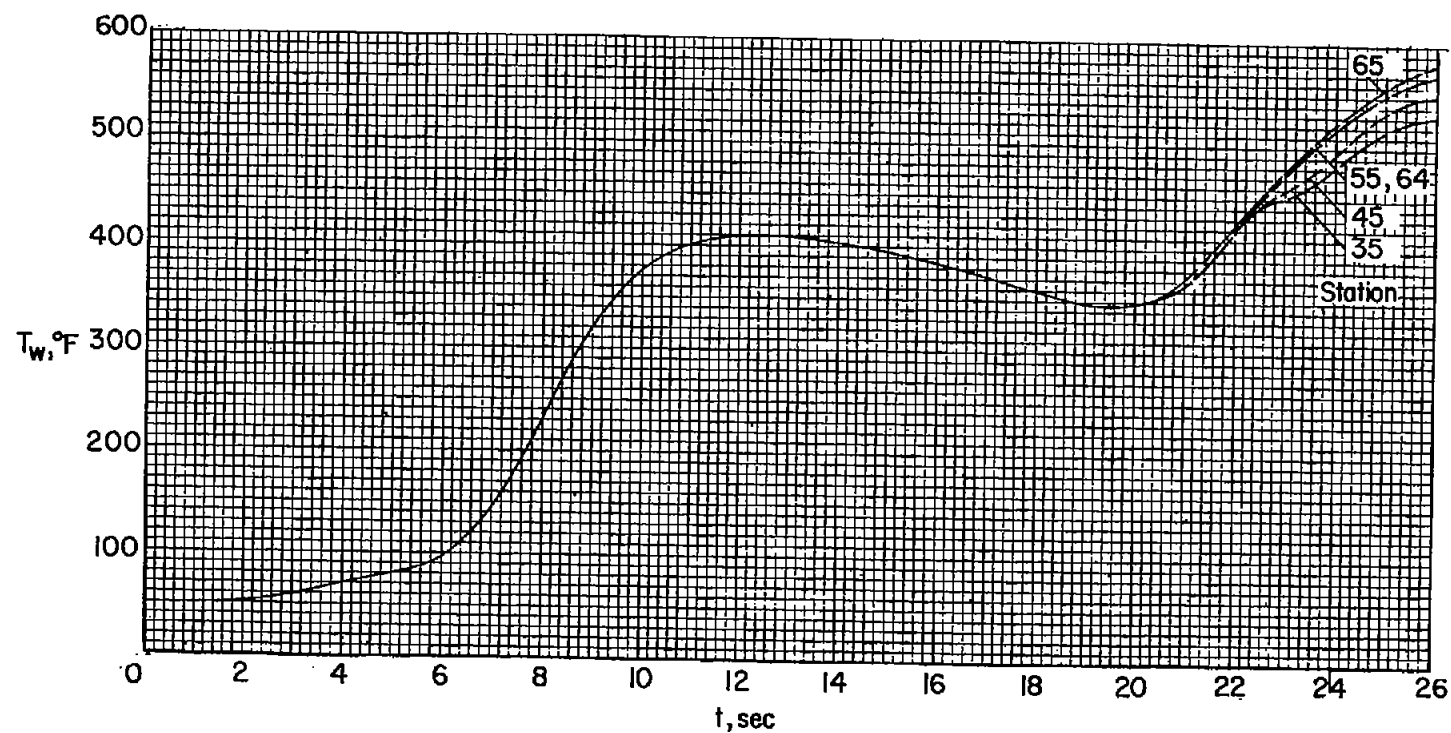
(b) Nose-cone stations 12.5, 14.0, 15.5, and 17.0.

Figure 4.- Continued.



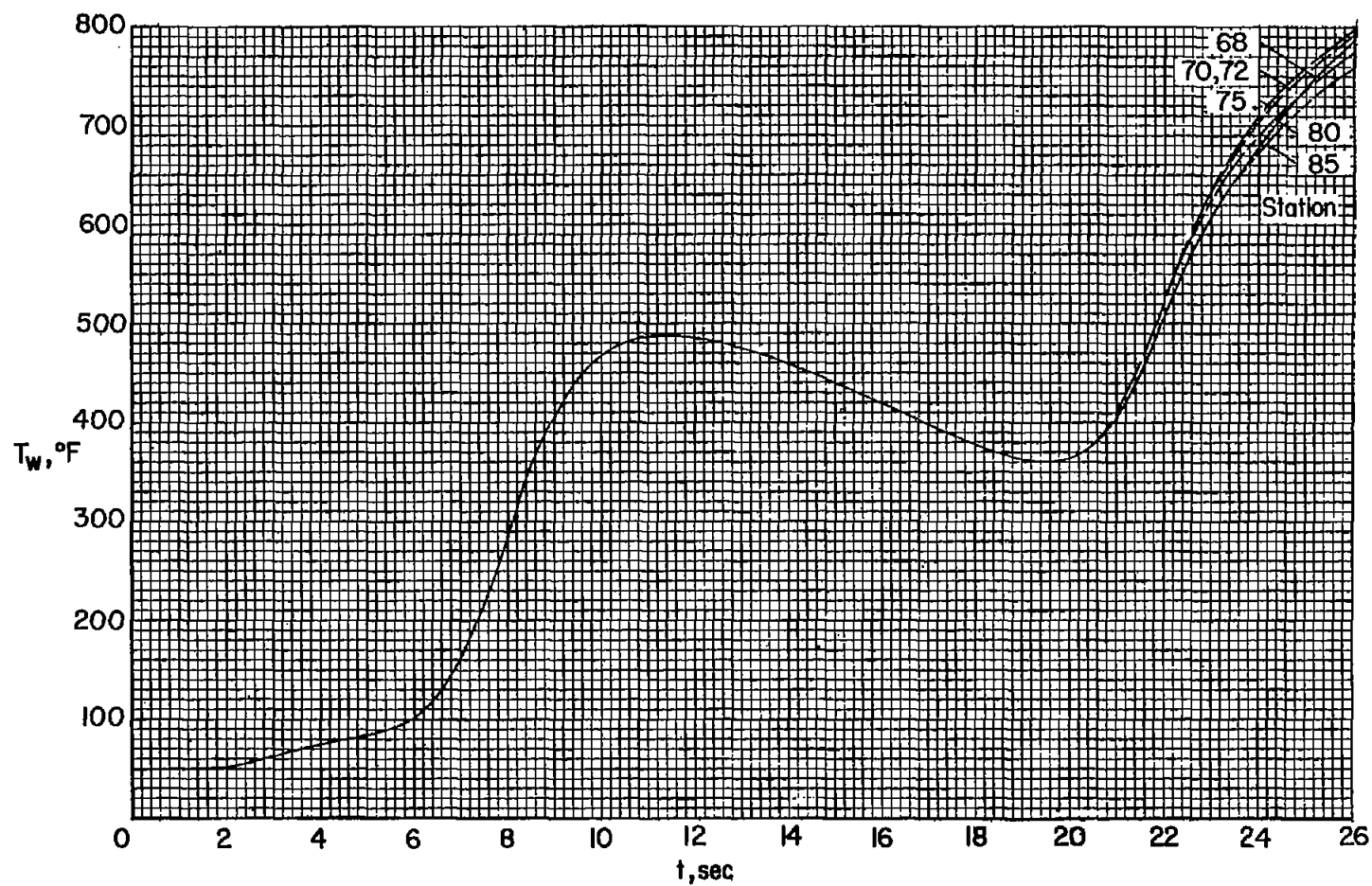
(c) Nose-cone stations 19.0, 21.0, 25.0, and 29.0.

Figure 4.- Continued.



(d) Cylinder stations 35.0, 45.0, 55.0, 64.0, and 65.0.

Figure 4.- Continued.



(e) Flare stations 68.0, 70.0, 72.0, 80.0, and 85.0.

Figure 4.- Concluded.

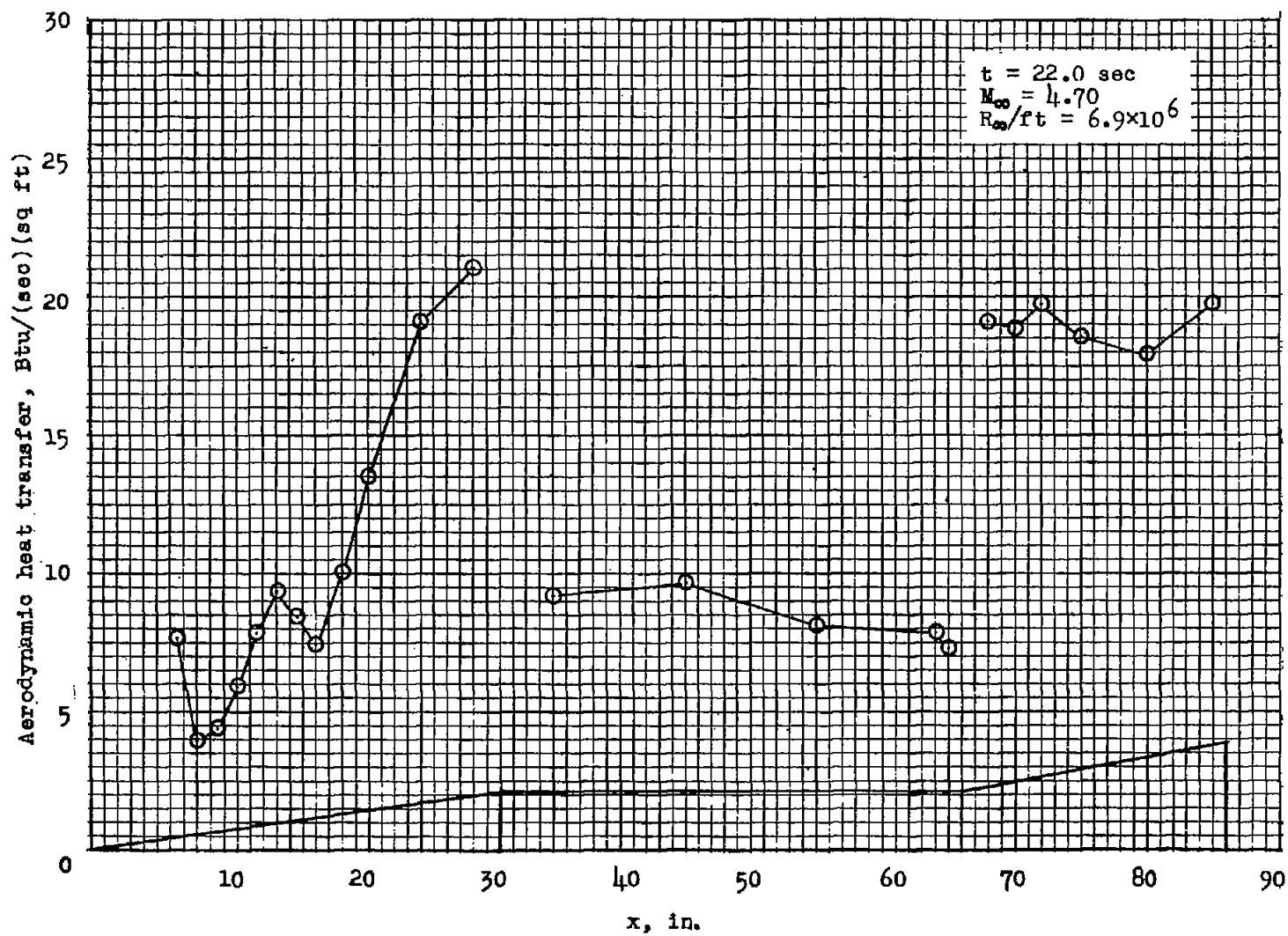


Figure 5.- Distribution of heat-transfer rates along the body at $t = 22.0$ seconds.

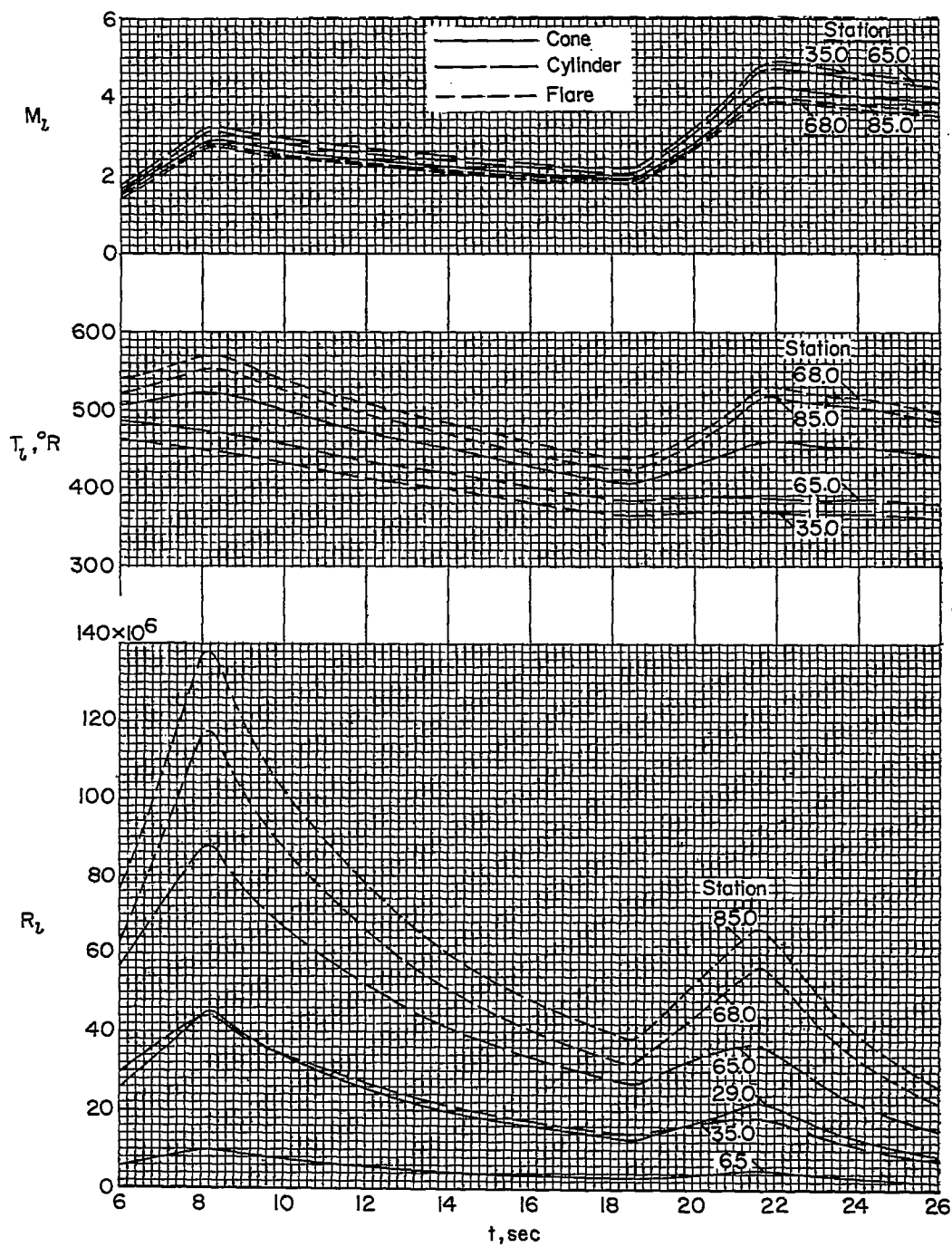


Figure 6.- Time histories of local flow conditions.

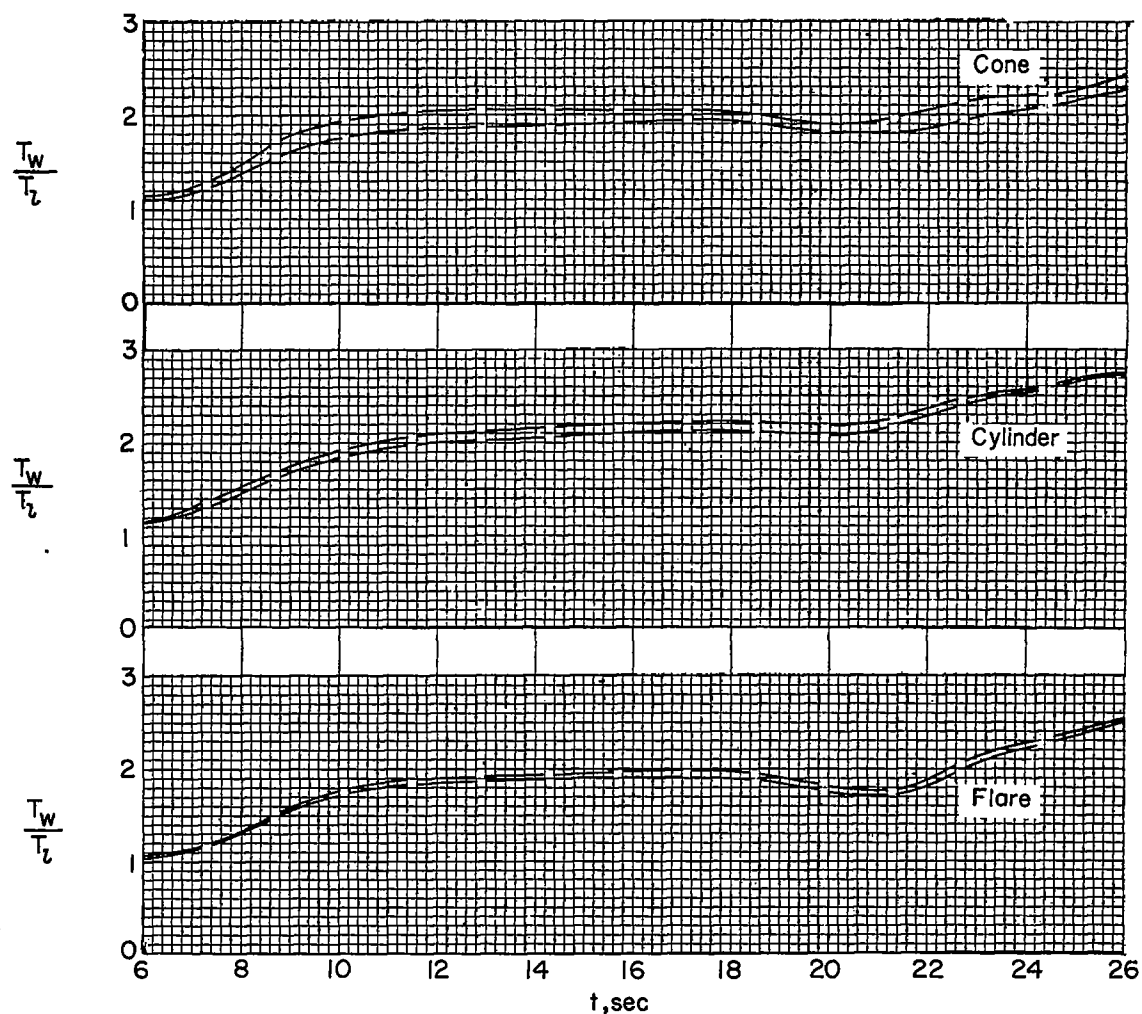
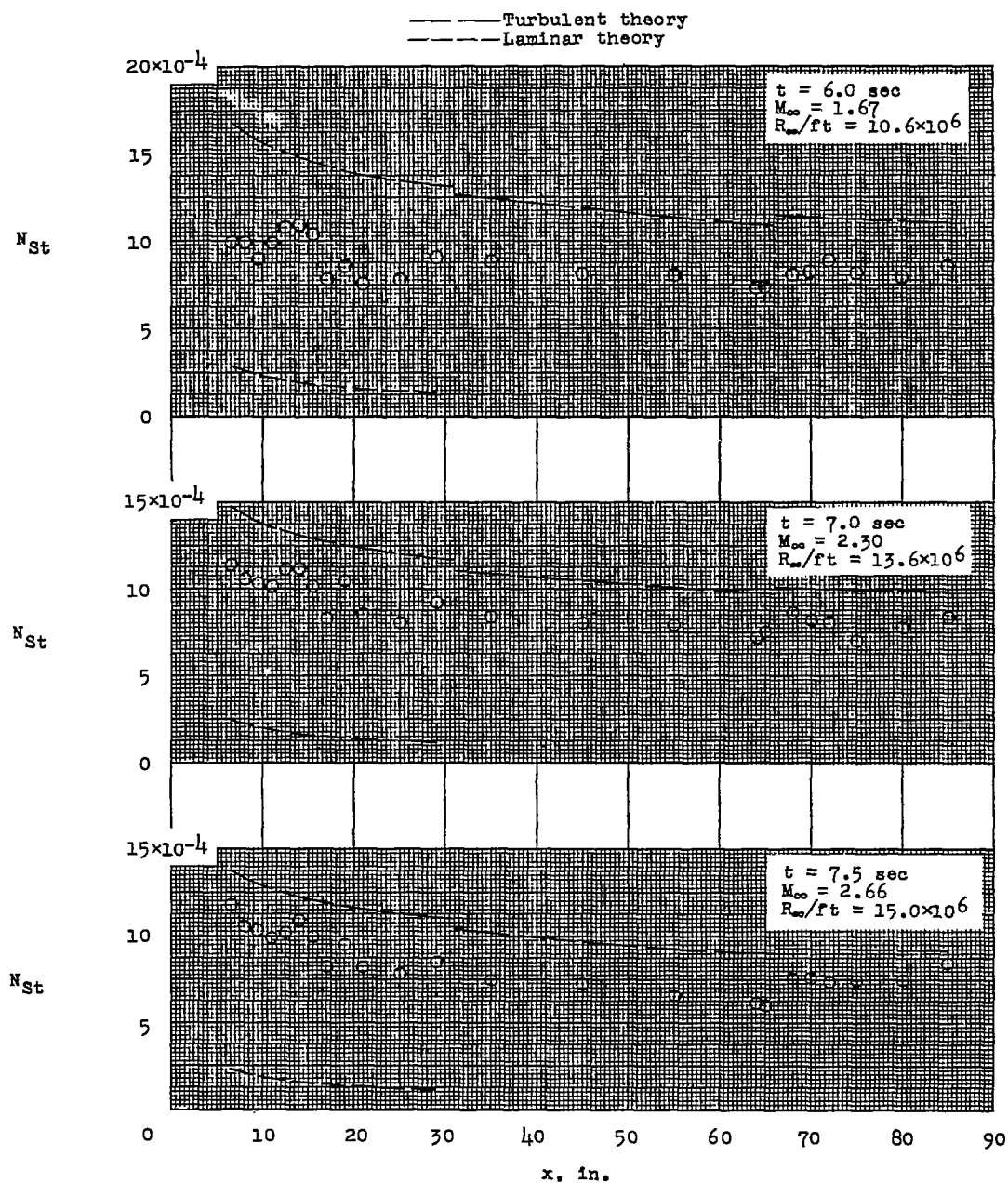
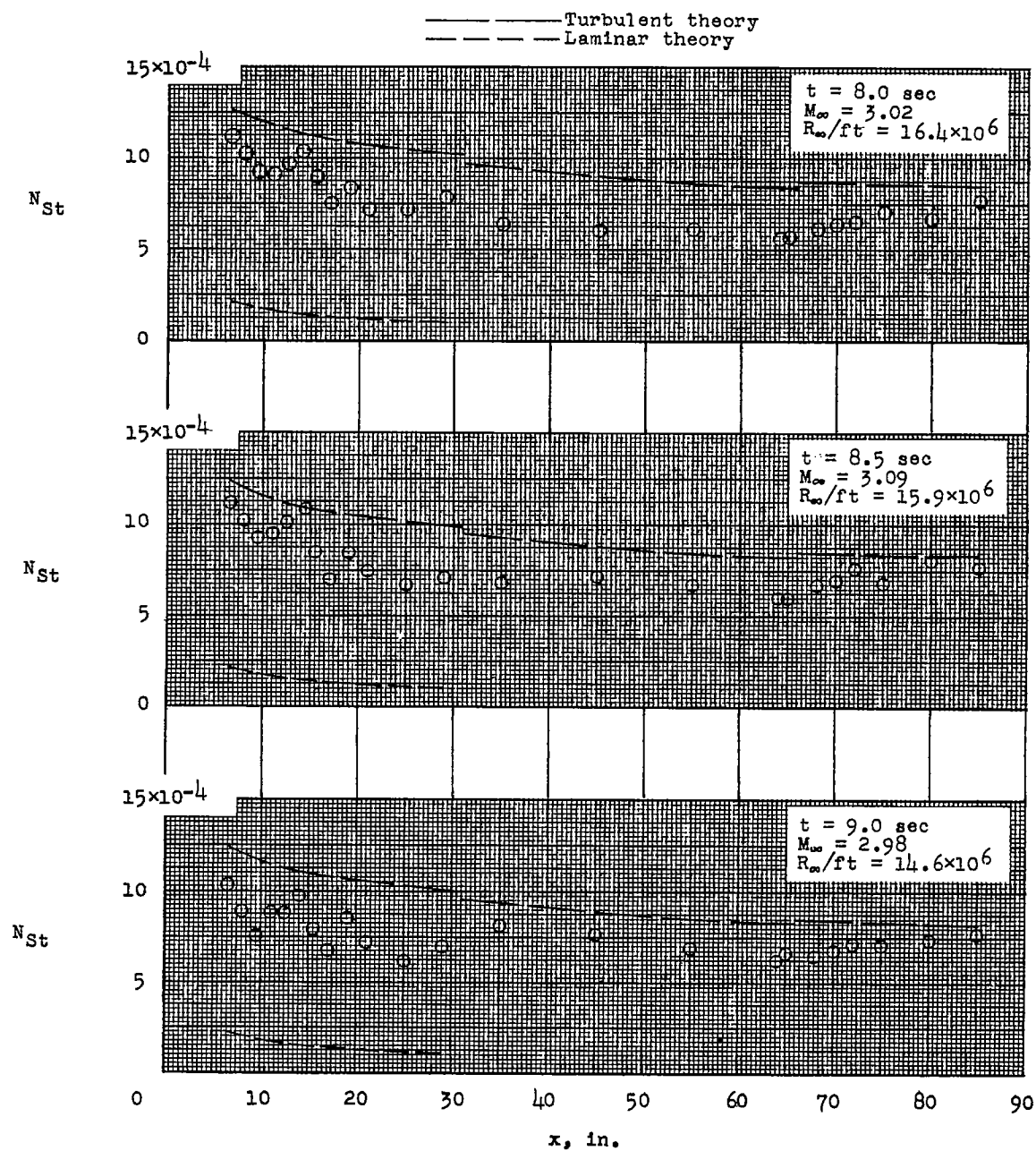


Figure 7.- Time histories of ratio of skin temperature to local static temperature.



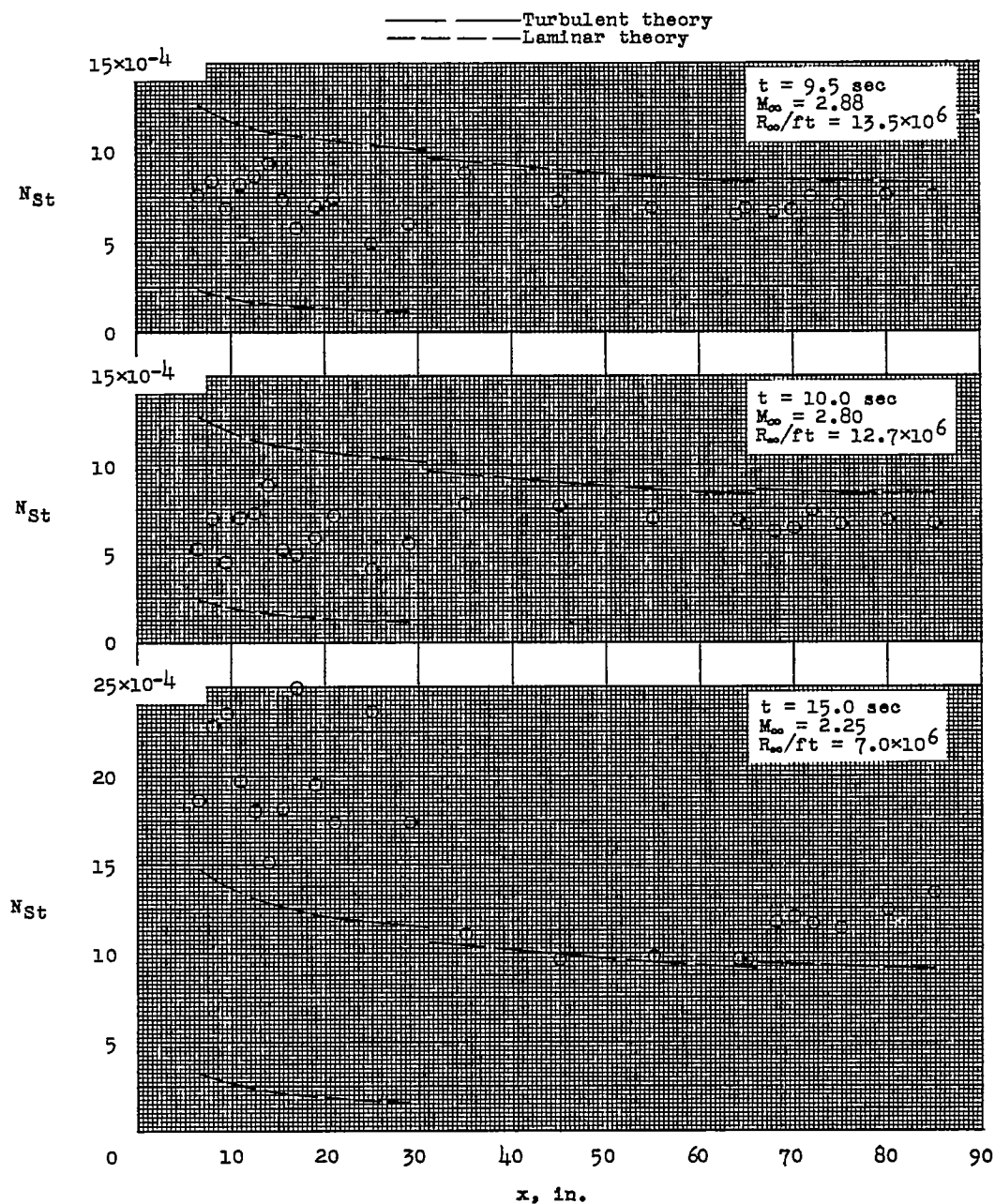
(a) Times 6.0, 7.0, and 7.5 seconds when $T_w < T_{aw}$, based on theoretical values of η_r .

Figure 8.- Distributions of Stanton number along body at several times.



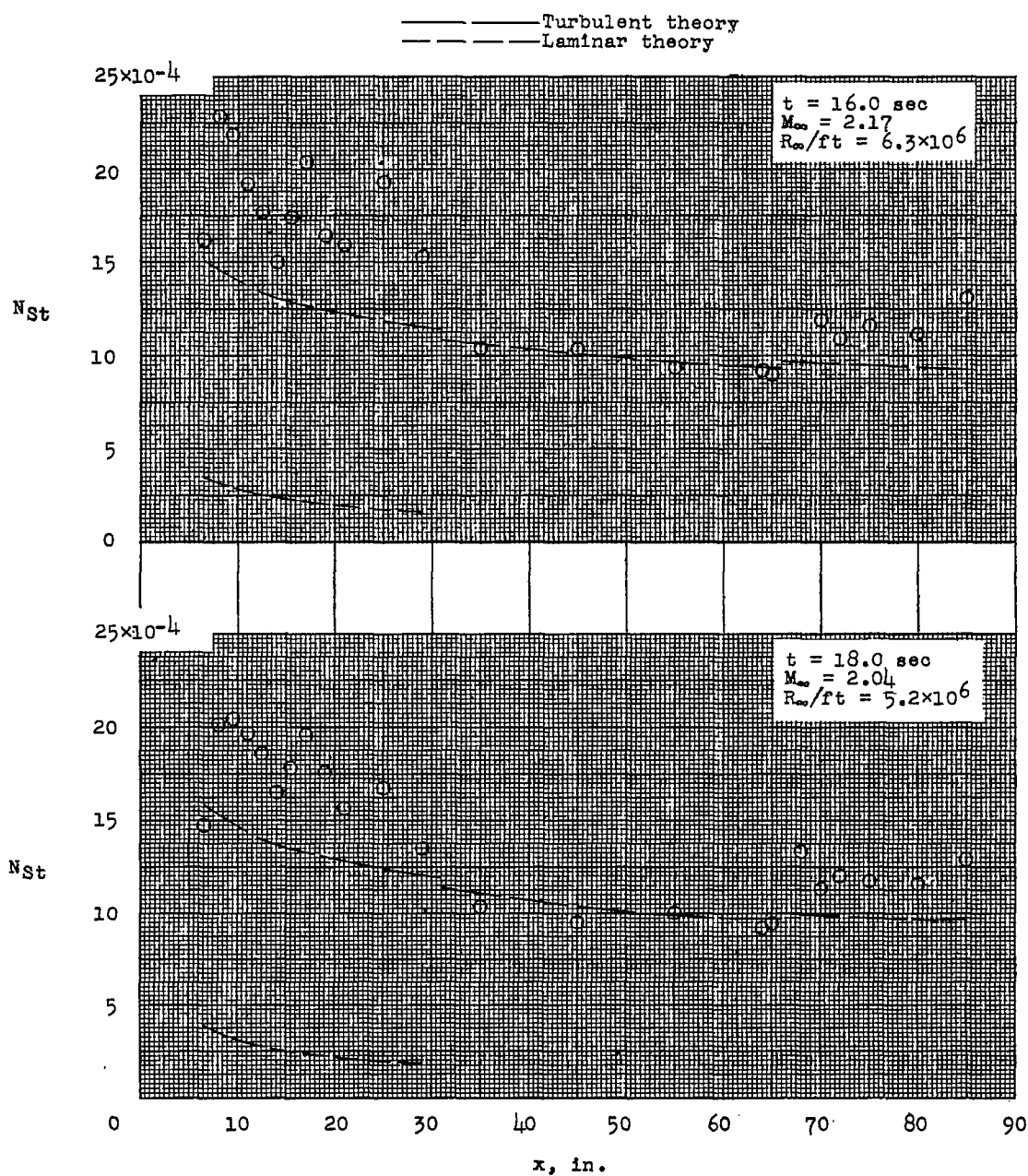
(b) Times 8.0, 8.5, and 9.0 seconds when $\bar{T}_w < T_{aw}$, based on theoretical values of η_r .

Figure 8.- Continued.



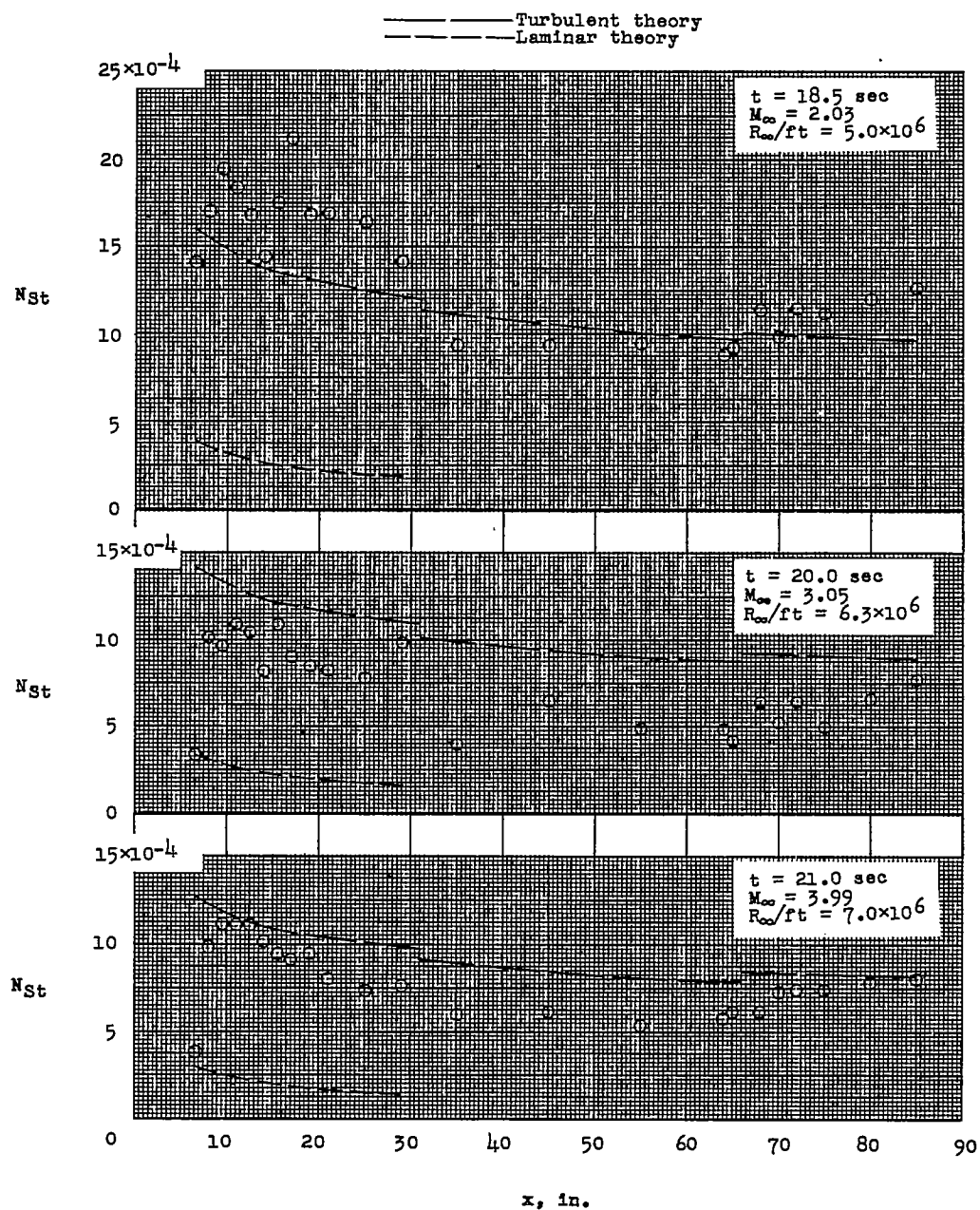
(c) Times 9.5 and 10.0 seconds when $T_w < T_{aw}$ and at 15.0 seconds when $T_w > T_{aw}$, based on theoretical values of η_r .

Figure 8.- Continued.



(d) Times 16.0 and 18.0 seconds when $T_w > T_{aw}$, based on theoretical values of η_r .

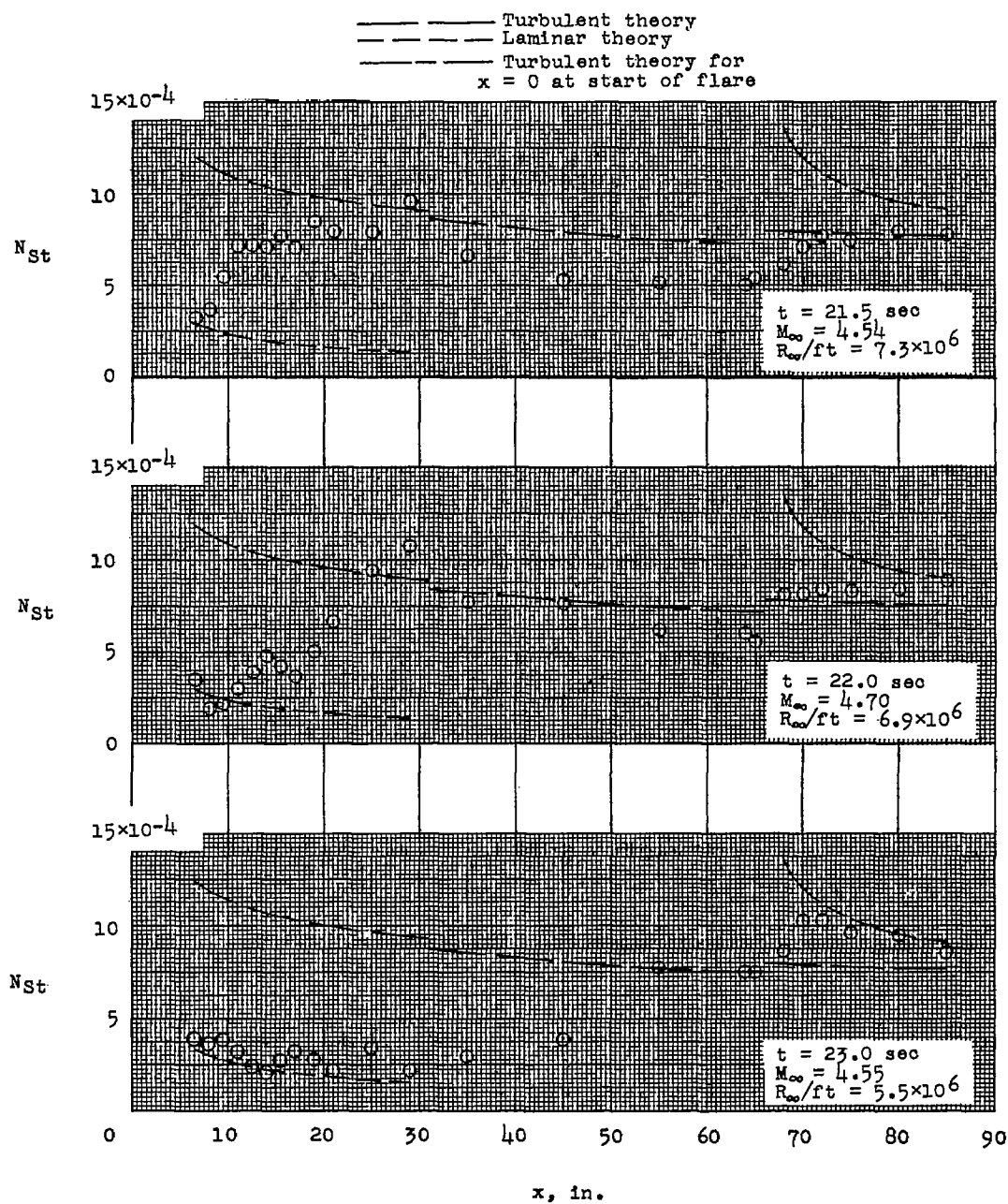
Figure 8.- Continued.



(e) Times 18.5 seconds when $T_w > T_{aw}$ and times 20.0 and 21.0 seconds when $T_w < T_{aw}$, based on theoretical values of η_r .

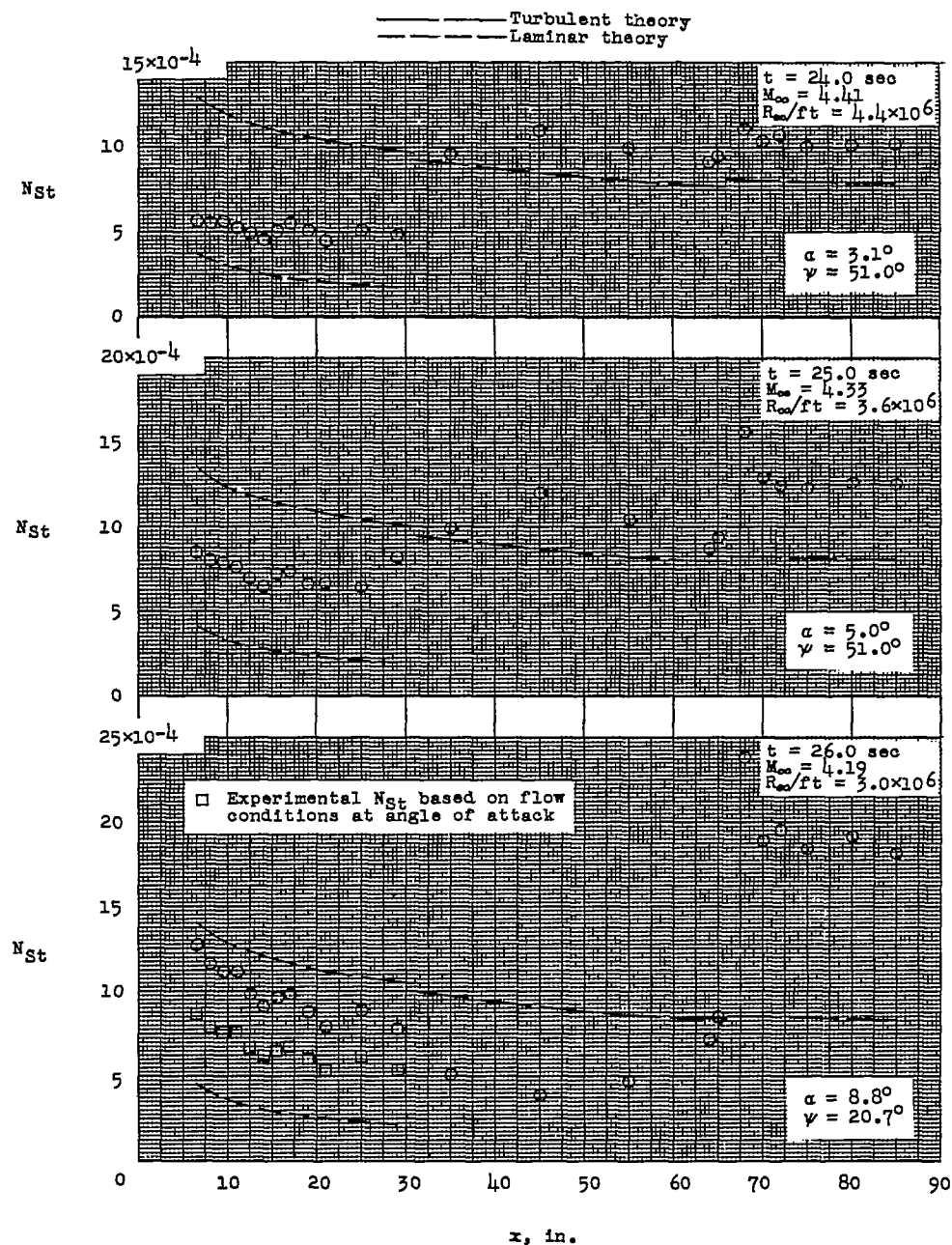
Figure 8.- Continued.

CONFIDENTIAL



(f) Times 21.5, 22.0, and 23.0 seconds when $T_w < T_{aw}$, based on theoretical values of η_r .

Figure 8.- Continued.



(g) Times 24.0, 25.0, and 26.0 seconds when $T_w < T_{aw}$, based on theoretical values of η_r .

Figure 8.- Concluded.

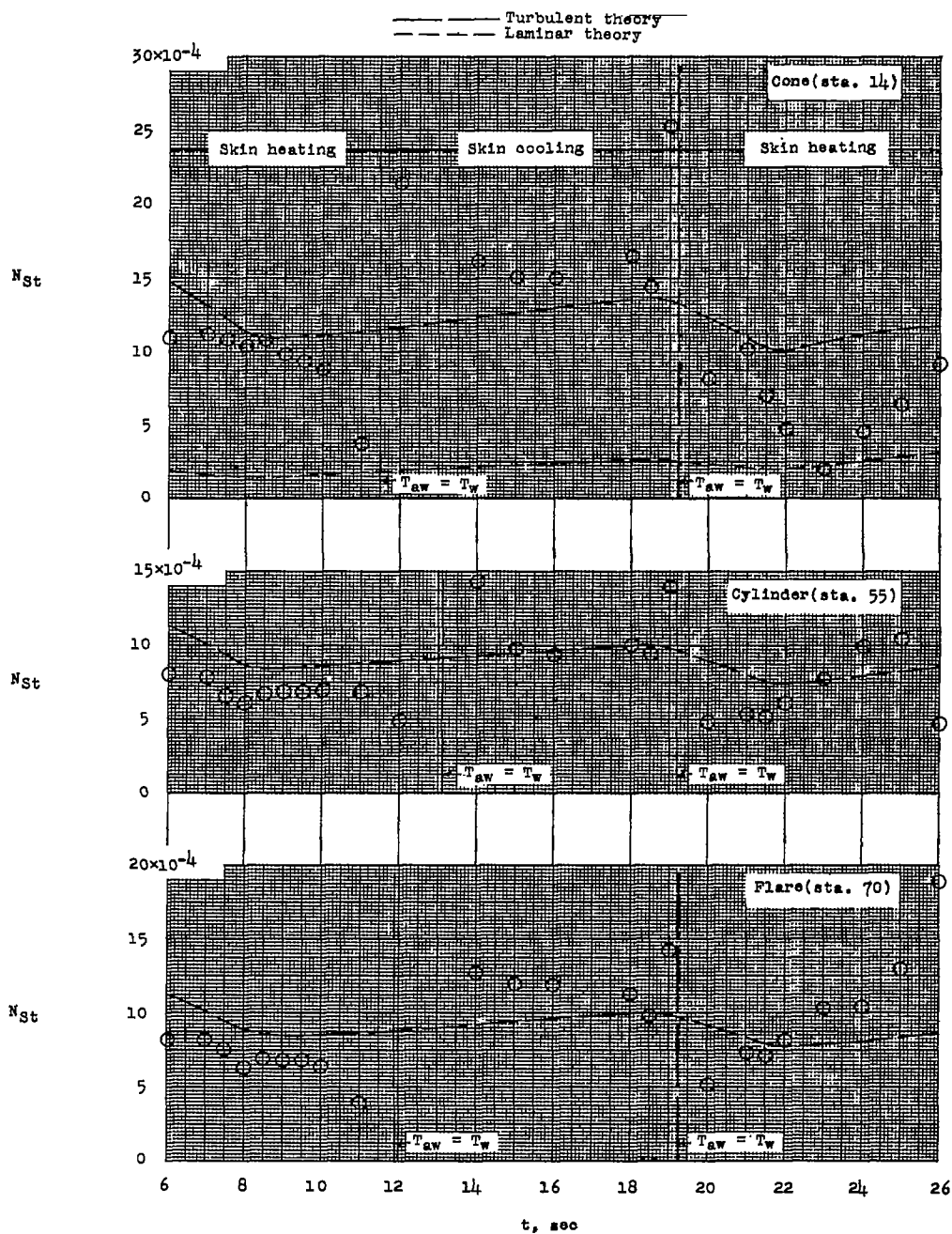
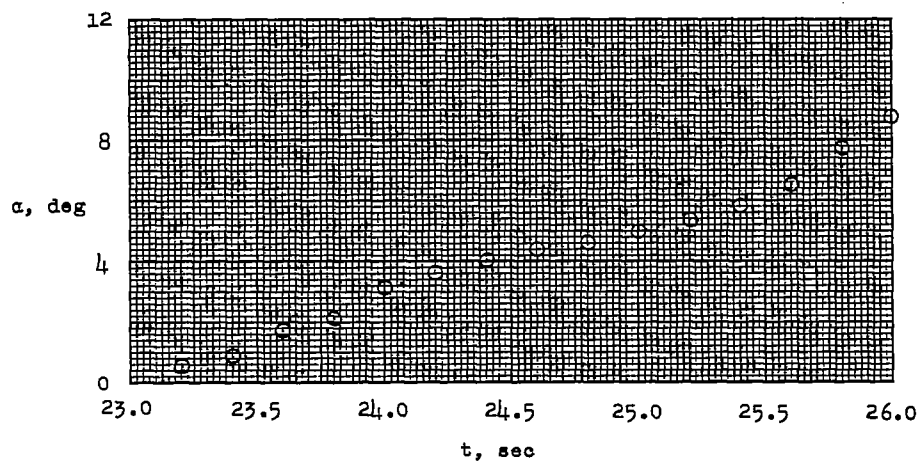
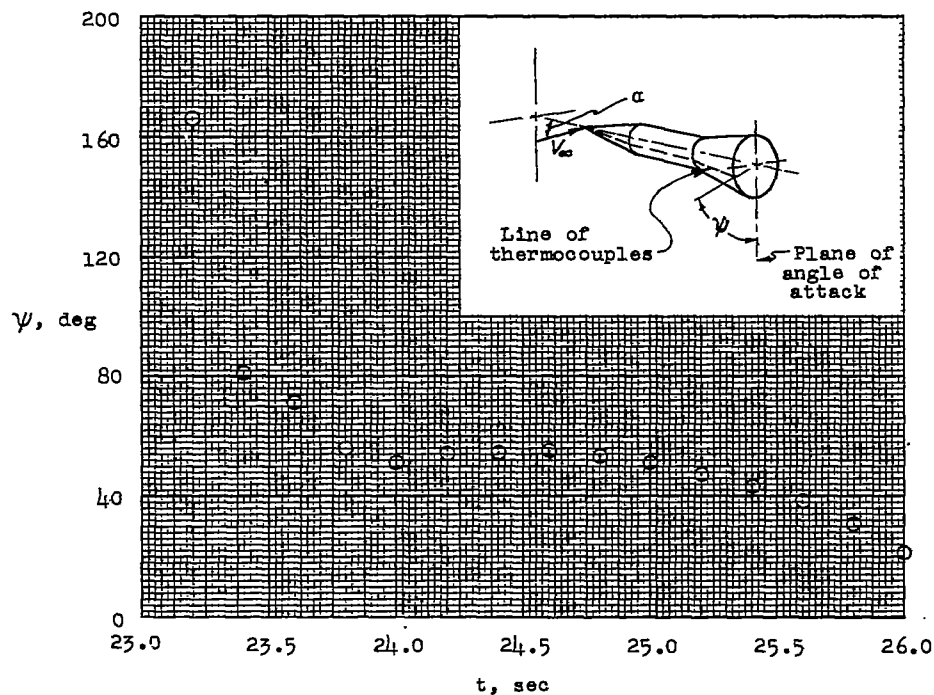


Figure 9.- Time histories of Stanton number based on theoretical values of η_r for three typical measurement stations.



(a) Variation of angle of attack α with time t .



(b) Orientation of thermocouple line.

Figure 10.- Variation of model attitude.

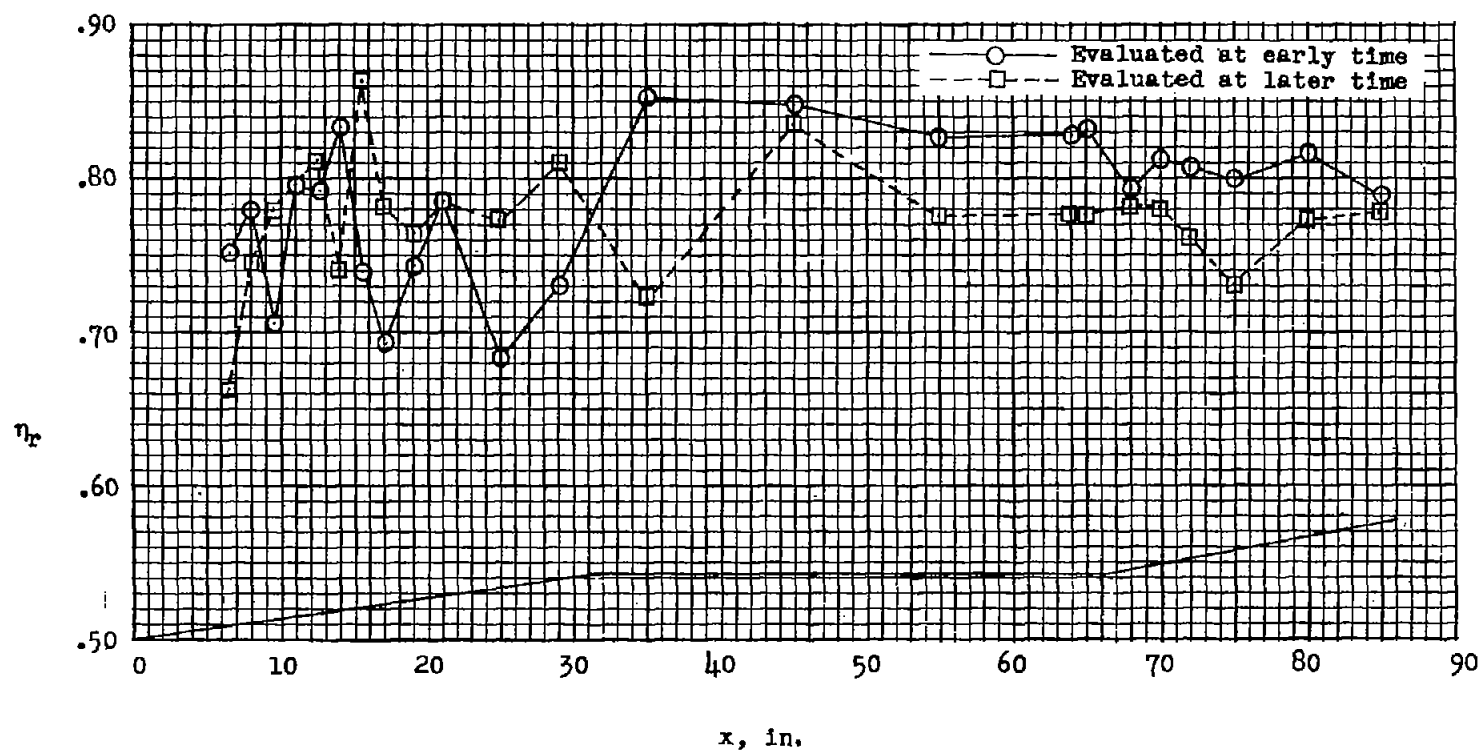


Figure 11.- Experimental recovery factors.

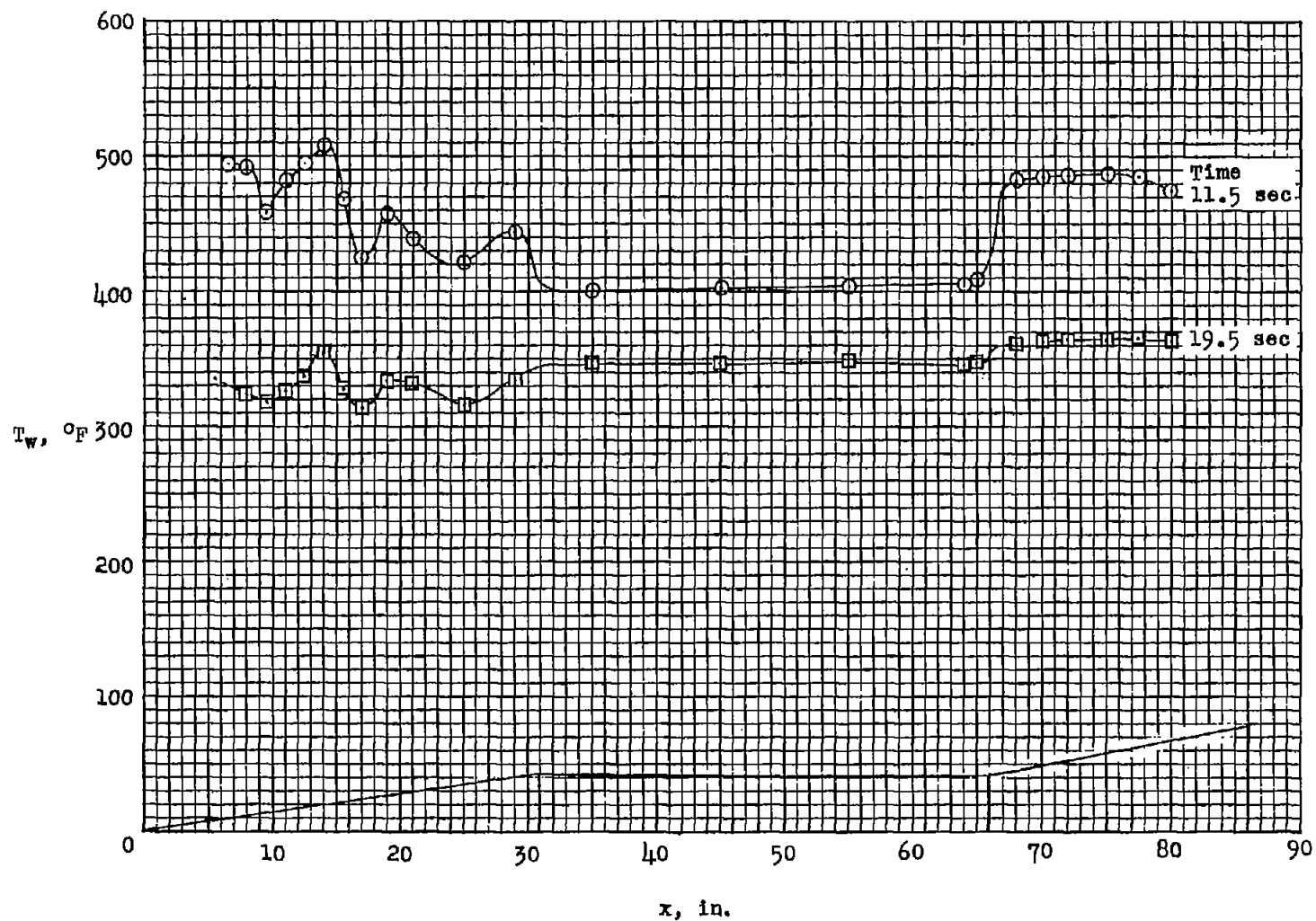


Figure 12.- Temperature distributions along body at times near experimental recovery factor evaluations.

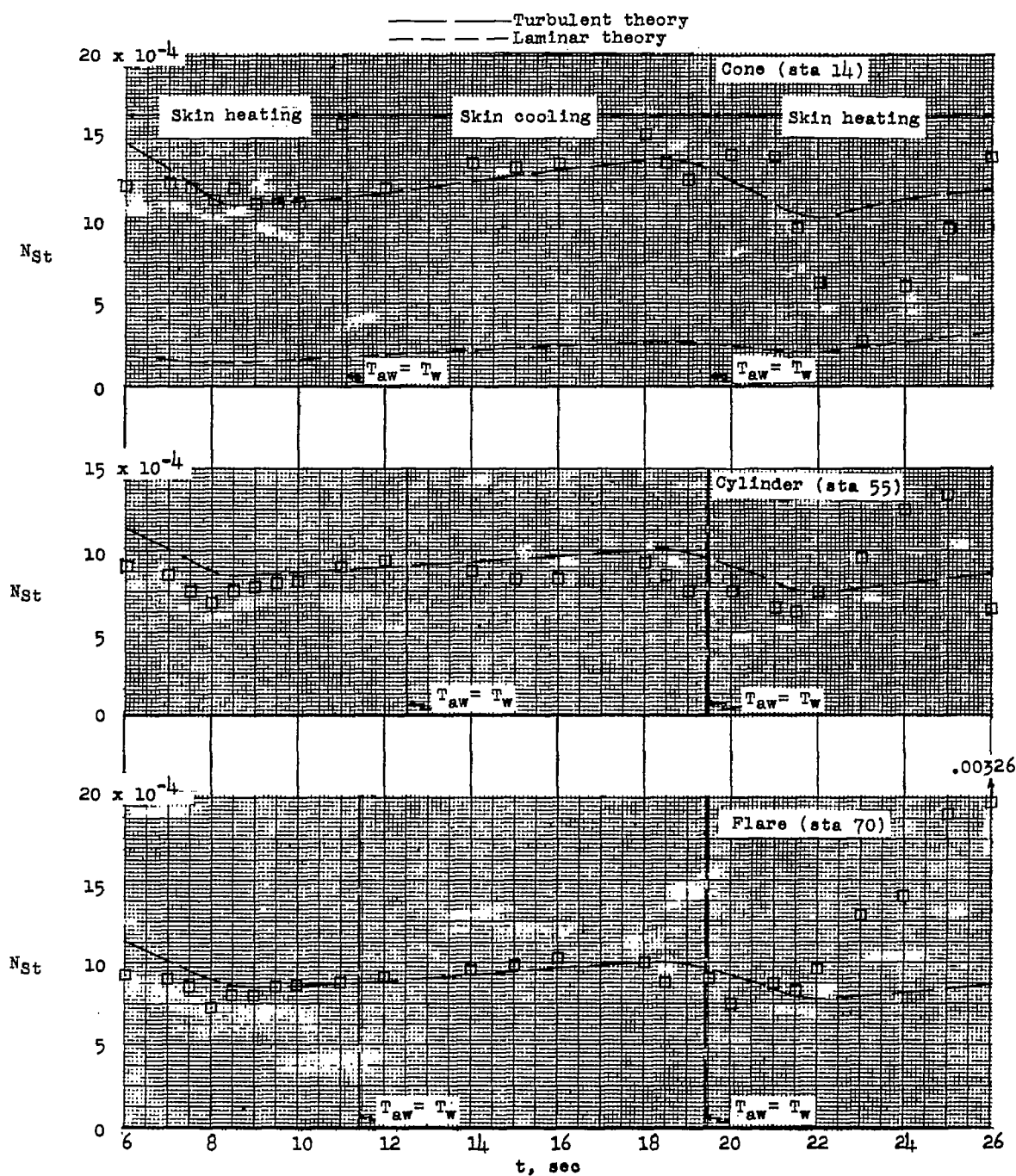
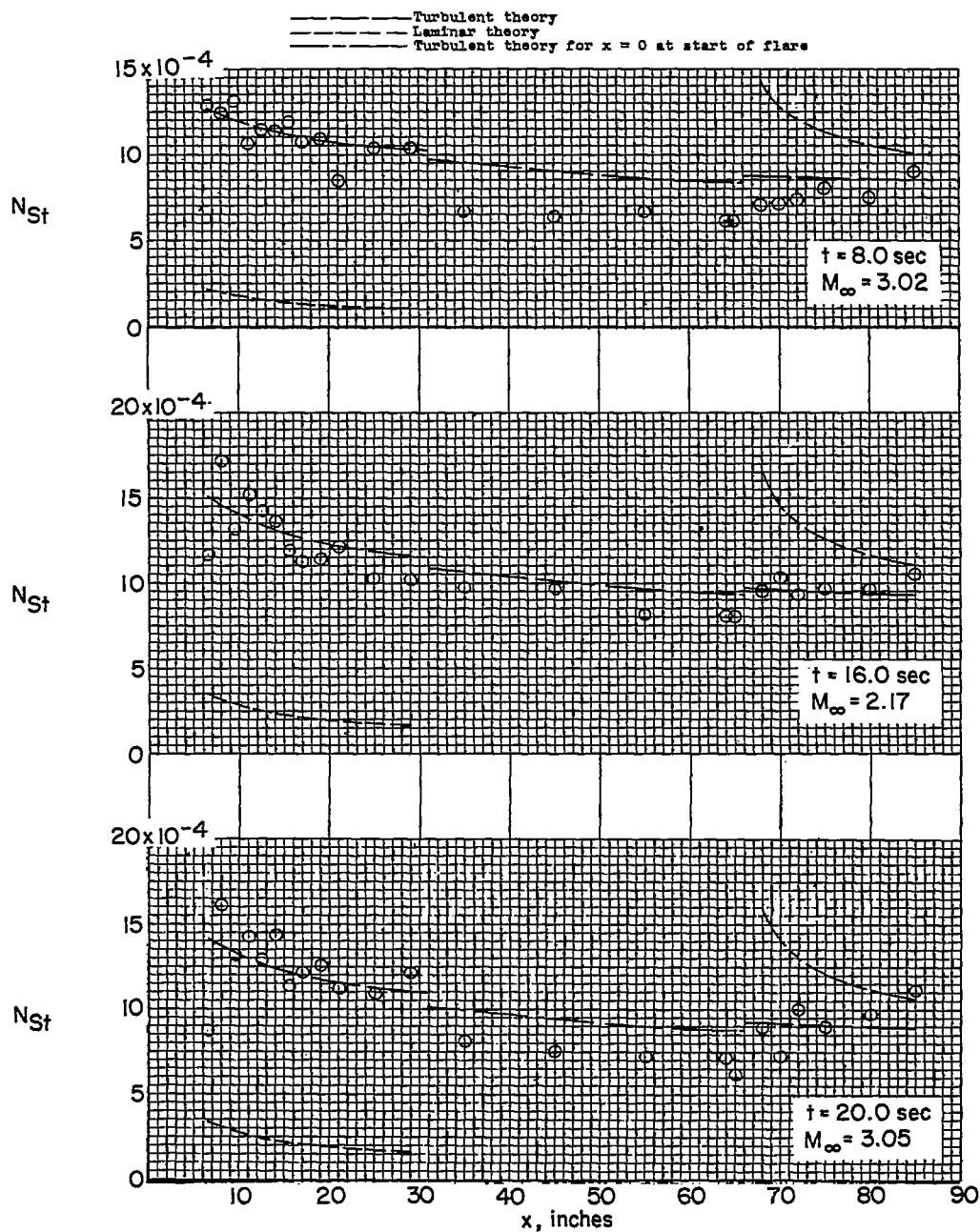
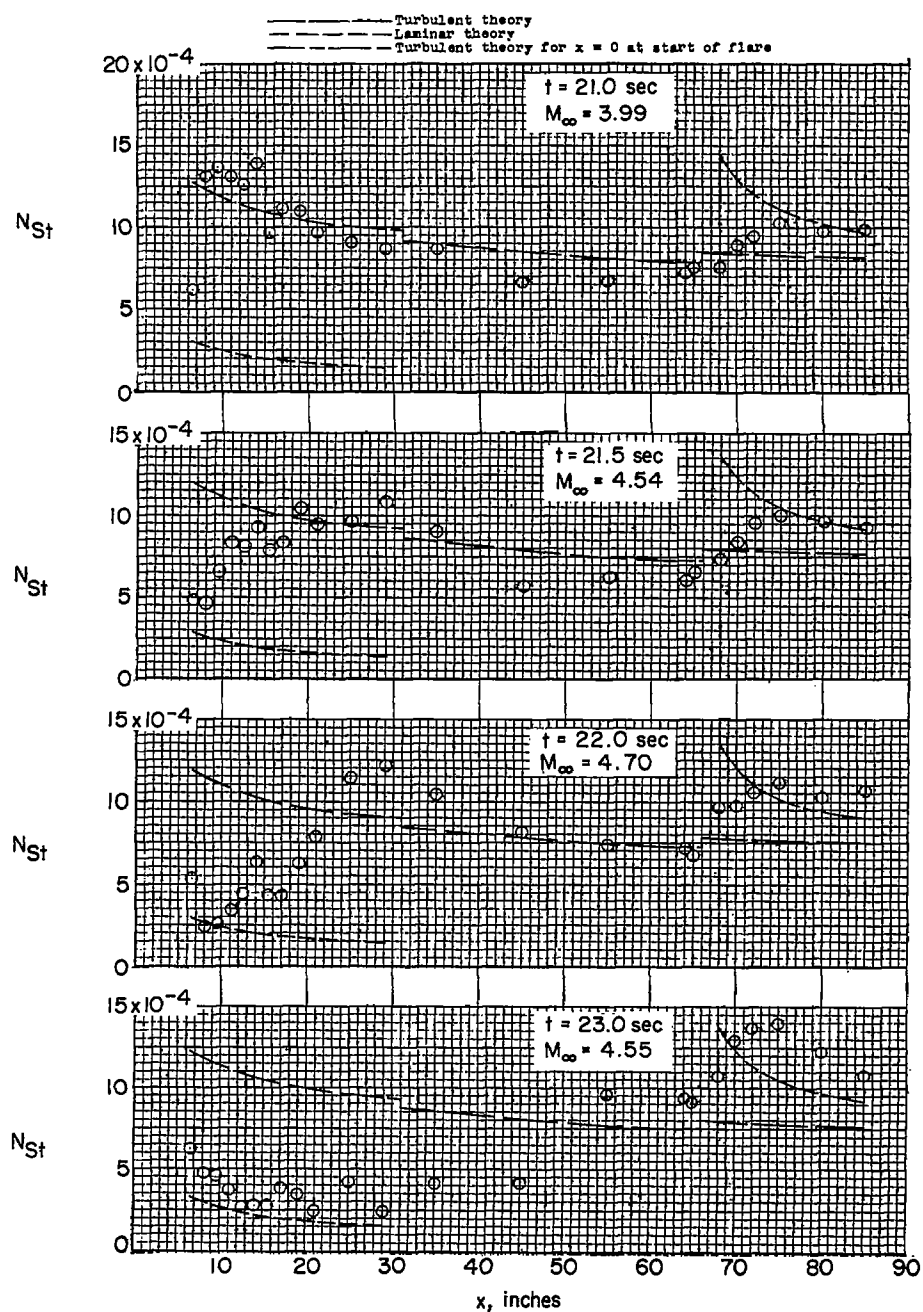


Figure 13.- Time histories of Stanton number based on experimental values of η_r for three typical measurement stations.



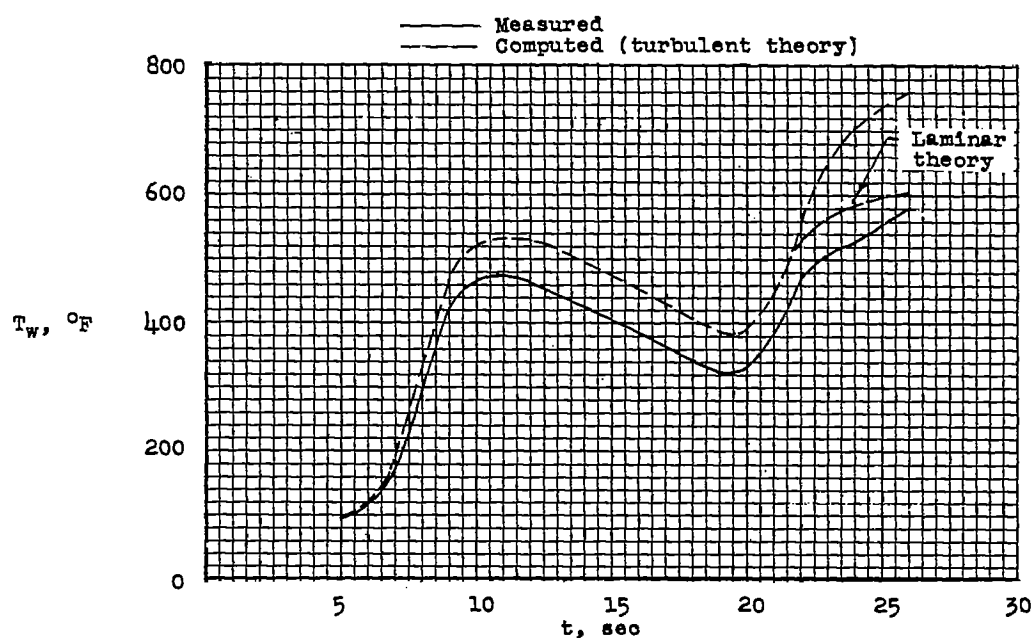
(a) Times 8.0, 16.0, and 20.0 seconds.

Figure 14.- Distributions of N_{St} based on experimental values of η_r .

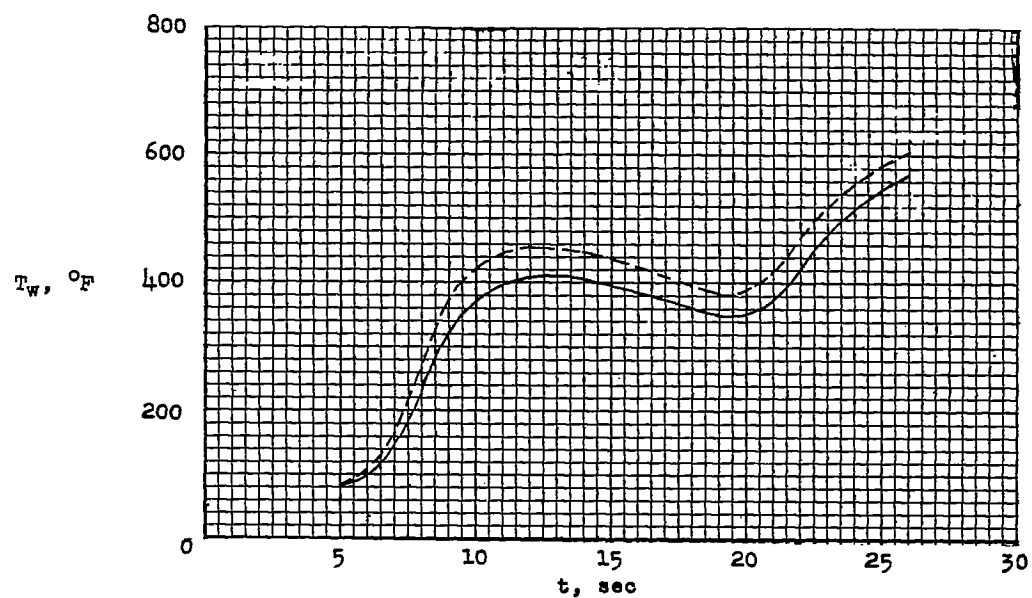


(b) Times 21.0 to 23.0 seconds.

Figure 14.- Concluded.

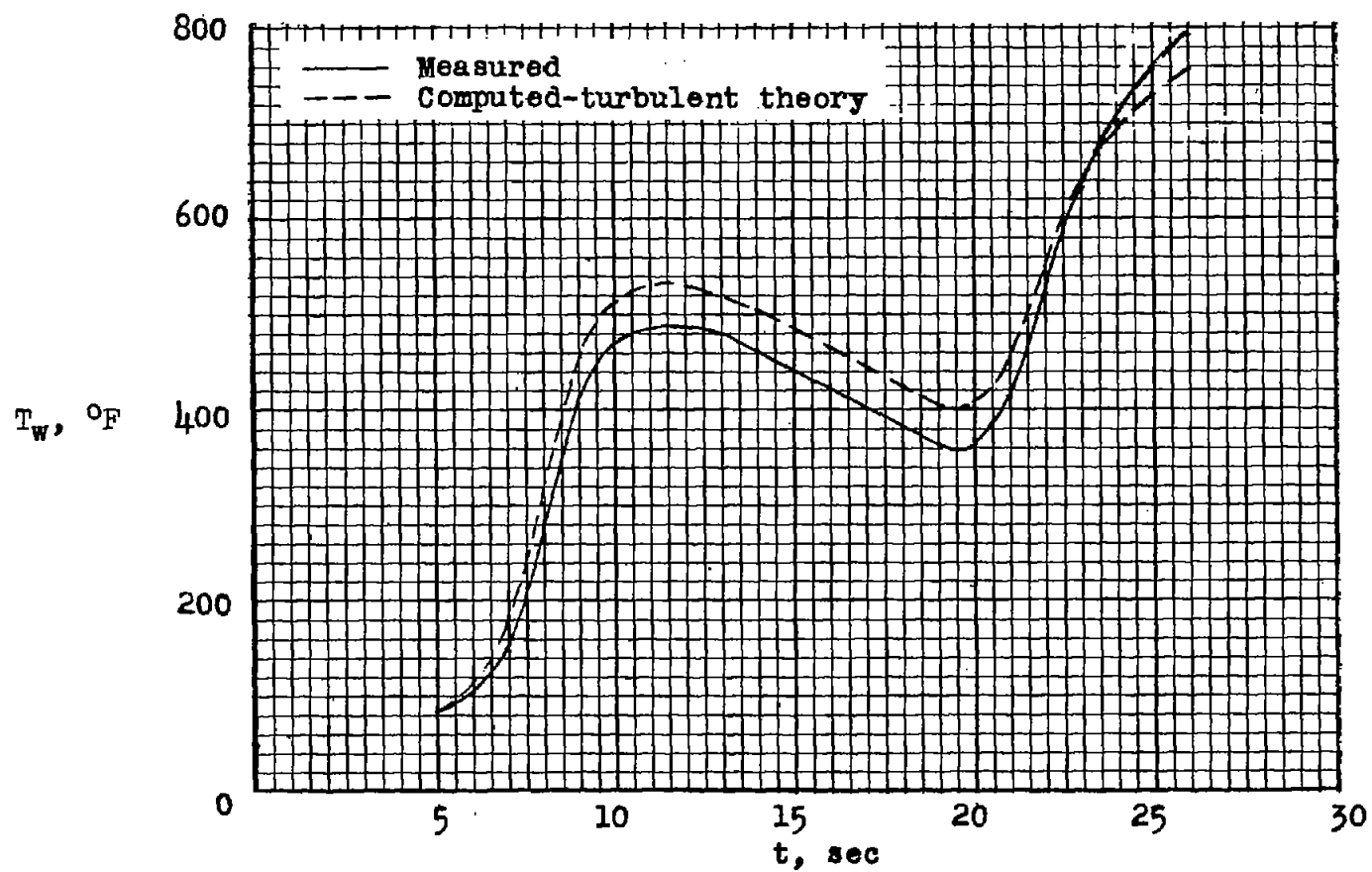


(a) Cone station 15.5.



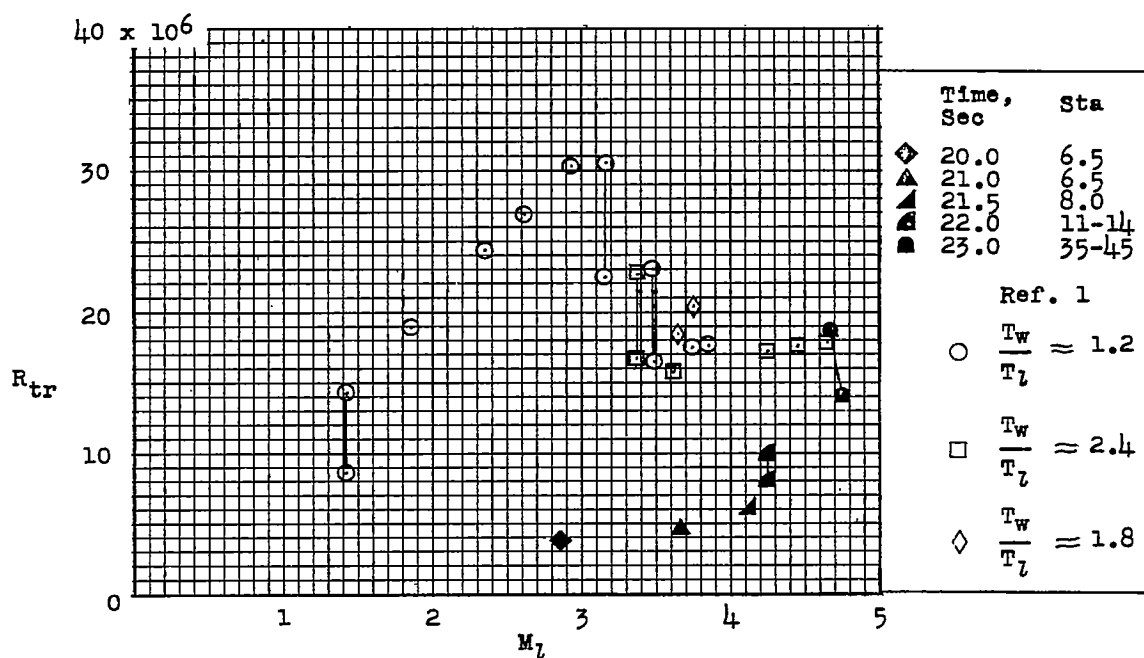
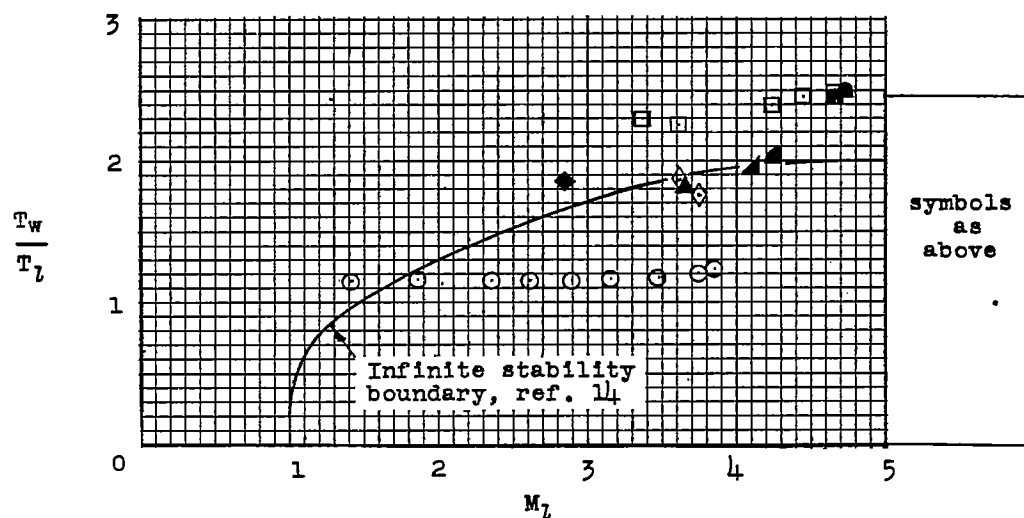
(b) Cylinder station 55.0.

Figure 15.- Comparison of measured and computed skin temperatures.



(c) Flare station 75.0.

Figure 15.- Concluded.

(a) R_{tr} as function of M_L .

(b) Conditions at transition.

Figure 16.- Boundary-layer transition measurements.

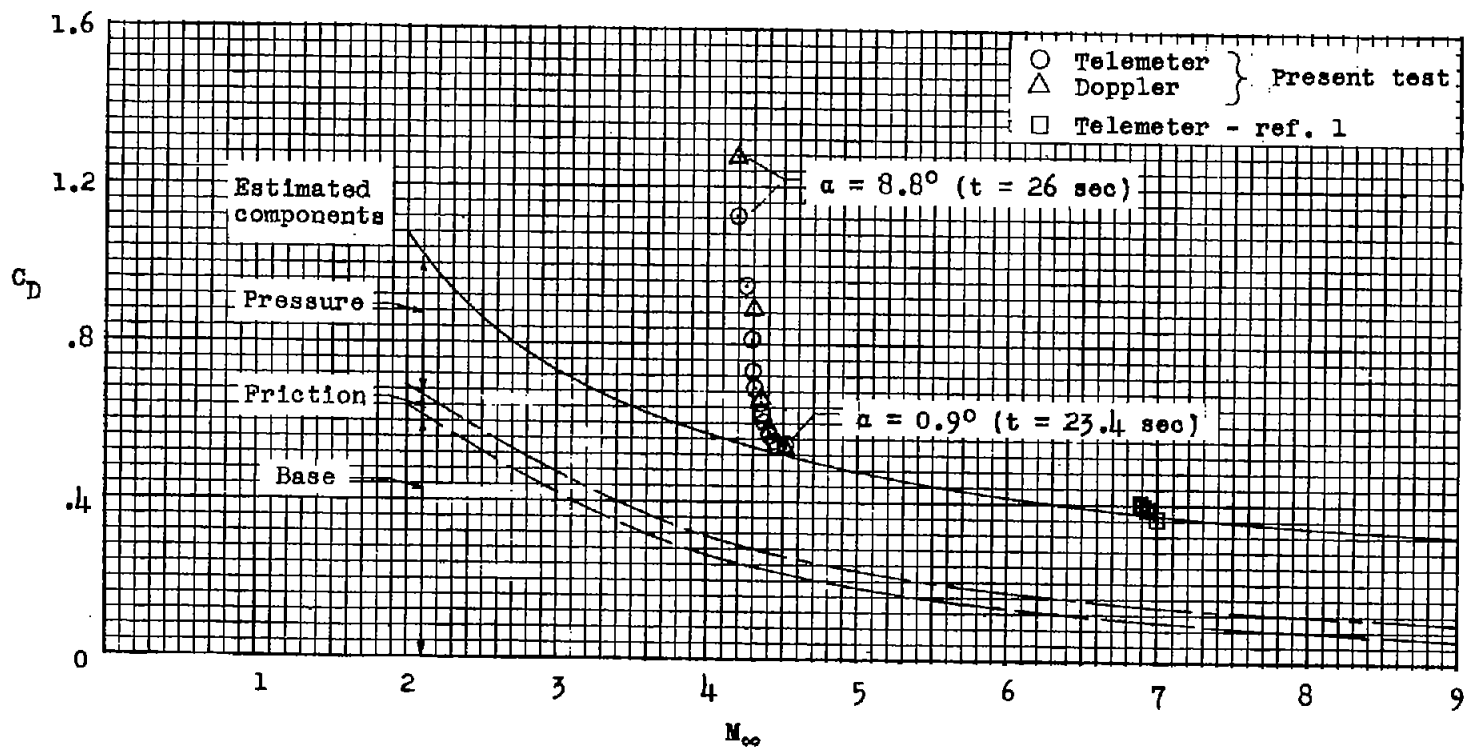


Figure 17.- Drag coefficients based on cylinder cross-sectional area.

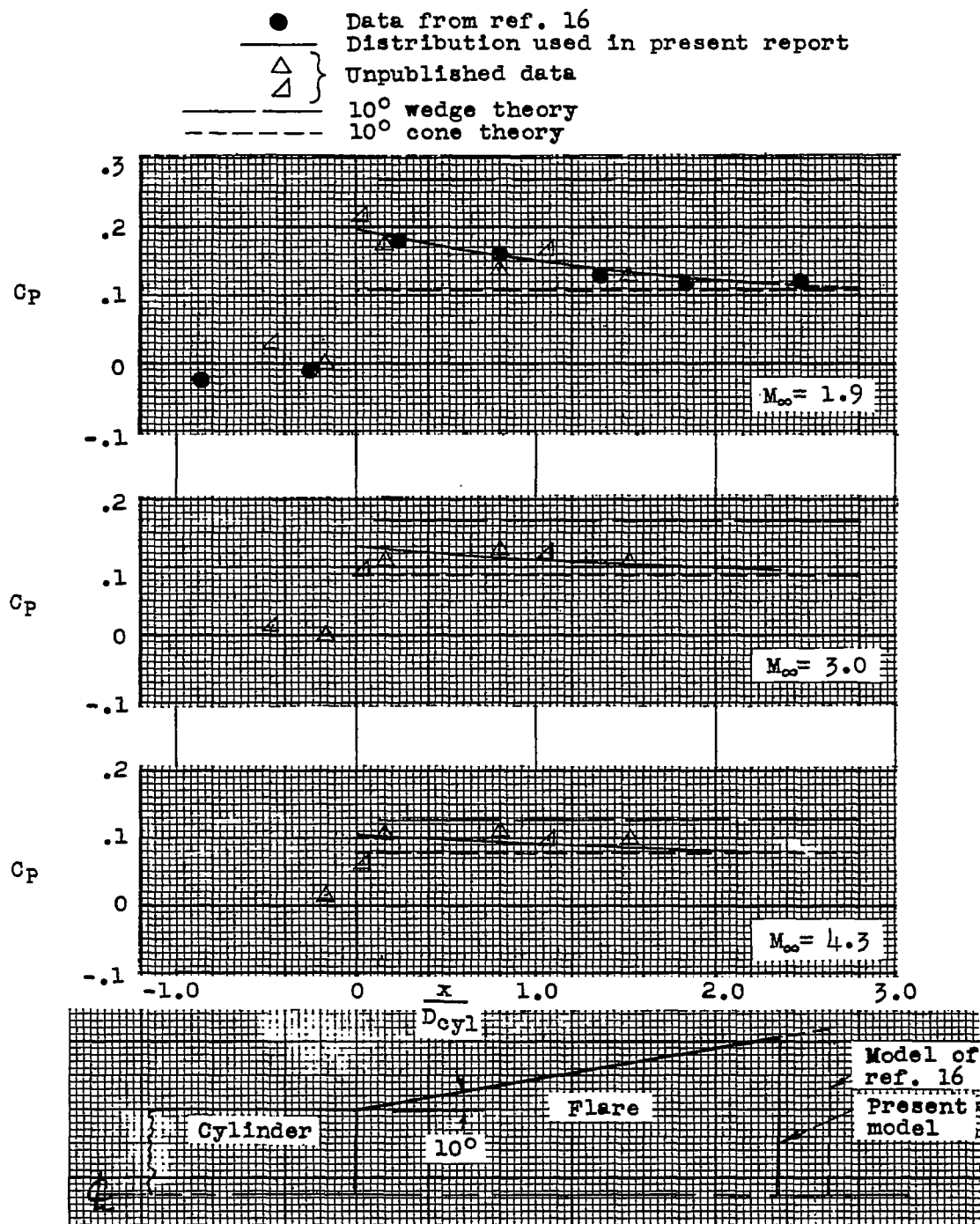
~~CONFIDENTIAL~~

Figure 18.- Pressure distributions along flare.

~~CONFIDENTIAL~~